1. Emission Lines in Nearby Galaxies

1.1. Models of Integrated Light of Galaxies

Models of galactic evolution including chemical evolution can be used to predict the continuous spectrum, absorption lines, and emission lines from the ISM as a function of assumed star formation history, IMF, age, and, with less importance (at least for massive galaxies), the time dependence of mass loss via galactic winds. Inputs also include evolutionary tracks (function of stellar mass, age, and metallicity, as well as mass loss history), nucleosynthesis yields (ranging from just studying some total metallicity to following each element individually). See the earlier discussion of chemical evolution models, both analytical and numerical, as well as the semi-analytical models which combine these factors with a cosmological hierarchical formation scenario.

1.2. Integrated Light of Galaxies – HII Region Emission Lines

The luminosity of massive stars is very high ($L \propto M^3$), and they tend to be clustered. Massive young star clusters (where high mass stars tend to reside) are detectable even in distant galaxies.

Interpreting the emission line spectrum in the integrated light requires understand the ionization field, both its total flux and its spectrum, both of which may be functions of position within the galaxy. The dominant contribution to the ionizing continuum in star-forming galaxies is massive stars. Knowledge of the IMF, the star formation history, metallicity, spatial distribution of dust and its reddening curve, are all needed to compute the ratios of the strength of various emission lines from the ISM occuring at different rest wavelengths.

Before proceeding to the emission lines themselves, we address the reddening (absorption of light by the intervening material, both through our galaxy and the IGM along the line sight, and within the galaxy of interest itself). Both of these are functions of wavelength, with more absorption at bluer wavelengths. Assuming the galaxy of interest is not close to the plane of the Milky Way, the first term is relatively small. The absorption within the source galaxy is a function of of the chemical composition and grain size distribution of the dust within the galaxy, of its spatial distribution, and of the angle of the galaxy with respect to the line of sight. Since absorption depends on dust, the reddening curve (the extinction as a function of wavelength) depends on the mean metallicity of the galaxy.

Complex scenarios arise. For example, in a starburst there are so many SN that they bubbles they each blow in the ISM merge together and remain relatively clear of gas. However, in normal star-forming galaxies, the star formation is less vigorous, it takes place in individual HII regions, not huge global complexes, and the HII regions individually do not output as much energy, and thus cannot clear the ISM around them. In this case, they will remain dust-enshrouded for a longer time than would be the case of a starburst. Because so much of the stellar emitted energy is absorbed by the dust, which then reradiates it in the IR, the bolometric IR emission from galaxies integrated in wavelength (from 5 to 1000 μ for example) is often used as an indicator of star formation. Another problem that is encountered in calculating interstellar absorption is that the stars that are responsible for the UV photoionizing flux are often physically separate rom the gas that produces the emission lines. See papers by Daniella Calzetti and collaborators, including her early work Calzetti, Kinney Storchi-Bergmann (1994, ApJ, 429, 582).

Emission lines from the hottest stars themselves (in addition to those from the ISM) can also sometimes be seen in the integrated light. An example is the Wolf-Rayet population

(Wolf-Rayet stars are highly evolved stars which have lost almost all of their outer envelope, so that nuclear processed material is exposed) with its broad emission features from stellar winds ("bumps"); the primary features are broad emission from HeII at 4686 Å and a red bump around 5700 Å.

The overall scheme is to use the stellar continuum spectrum to get the age of the cluster and derive the number of ionizing photons. Then subtract out the stellar component of integrated galaxy spectrum; the residual is the nebular spectrum. Then one fits the relative intensities of various emission lines to get the metallicity of the species giving rise to each transition. The one must correct the species abundance to the element abundance through knowledge of the ionization. These models have many parameters, inner and outer radii of HII regions, etc. Codes such as STARBURST99 by Claus Leitherer or the Pegase code are often used for this purpose to determine the stellar spectrum, while the photoionization code CLOUDY by Gary Ferland analyzes the emission line spectrum. More sophisticated codes are under development that couple the chemical to the spectral energy distribution of starburst galaxies by incorporating a star formation and a metallicity evolution given by a chemical evolution code (see, e.g. Martin-Manjon, Molla, Diaz & Terlevich, 2008, arXiv:0810.2162).

An observational issue is correctly finding the emission line luminosity, since any underlying stellar continuum emission or line absorption must be removed; the latter is particularly troublesome for the Balmer lines, which are strongly in absorption in the stellar component, and in emission from the gas. Disentangling the two contributions is sometimes difficult.

The first thing to determine is whether the emission spectrum arises from gas photoionized by dilute starlight or by an AGN with a much harder ionizing spectrum. Of course, if the emission lines are very broad, then they must arise via an AGN. But

for narrow lines, we need some way to separate the two. The usual AGN diagnostic is based on line ratios which are sensitive to the hardness of the photoionizing spectrum such as [NII]/Hα (or [SII]/Hα) vs [OIII]/Hβ (the "Baldwin diagram", Baldwin, Phillips & Terlevich, 1981, PASP, 93, 5). Note that these line pairs are close together in wavelength so that the ratio is at least approximately independent of reddening.

For distant galaxies, the detectability of AGN emission in the integrated light may be reduced due to an aperture effect. Spectrographs usually operate with a slit approximately matched to the seeing. For a more distant galaxy, the spatial resolution at the source will correspond to a larger physical size, as compared to a well resolved nearby galaxy, where even the central regions can be studied in detail. This will lead to dilution of the AGN dominated light in the integrated light spectrum of a distant galaxy, reducing the apparent fraction of AGNs. Always be aware of possible observational or sample selection effects.

Table 1. Ionization Potentials of Key Elements

Elements	Neutral (eV)	Singly Ionized (eV)	Doubly Ionized (eV)
H	13.6	···	···
He	24.6	54.4	···
N	14.5	29.6	47.4
O	13.6	35.1	54.9
S	10.4	23.3	34.8

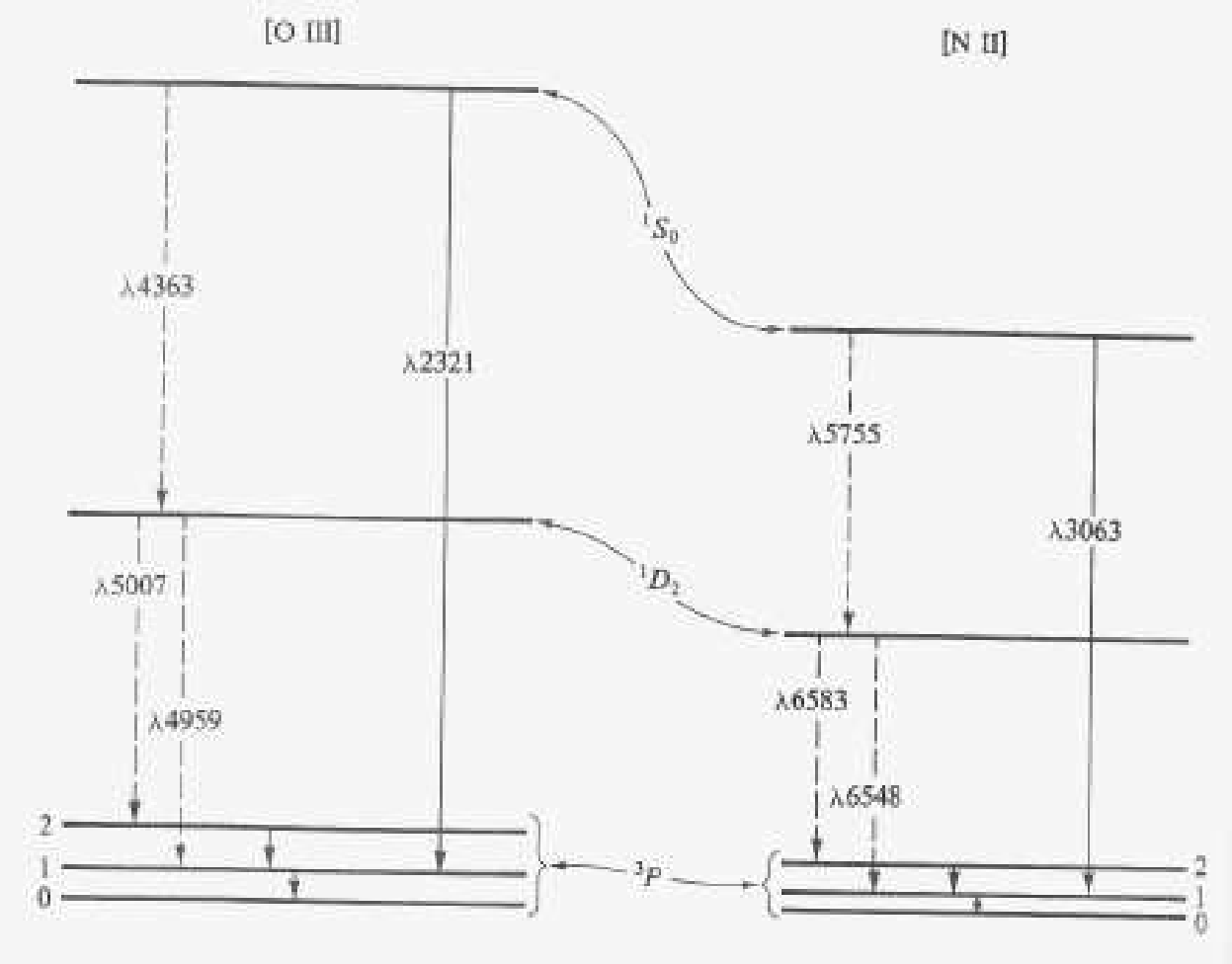

Fig. 1.— The energy level diagram for the lowest terms of [OIII], all from the ground state $2p^2$, and for [NII] of the same isoelectronic sequence. Splitting of the ground ^3P term has been exaggerated for clarity. Emission lines in the optical region are indicated by dashed lines, those in the IR or UV by solid lines. Only the strongest transitions are indicated. Note the key lines of [OIII] at 4363, 4959, and 5007 Å, and how the combination of the 4363 and 5007 Å indicates the excitation temperature. Unfortunately most of the time, the 4363 Å line is very weak and difficult to detect. (Fig. 3.1 of Osterbrock's book *Astrophysics of A Gaseous Nebulae and Active Galactic Nuclei*)

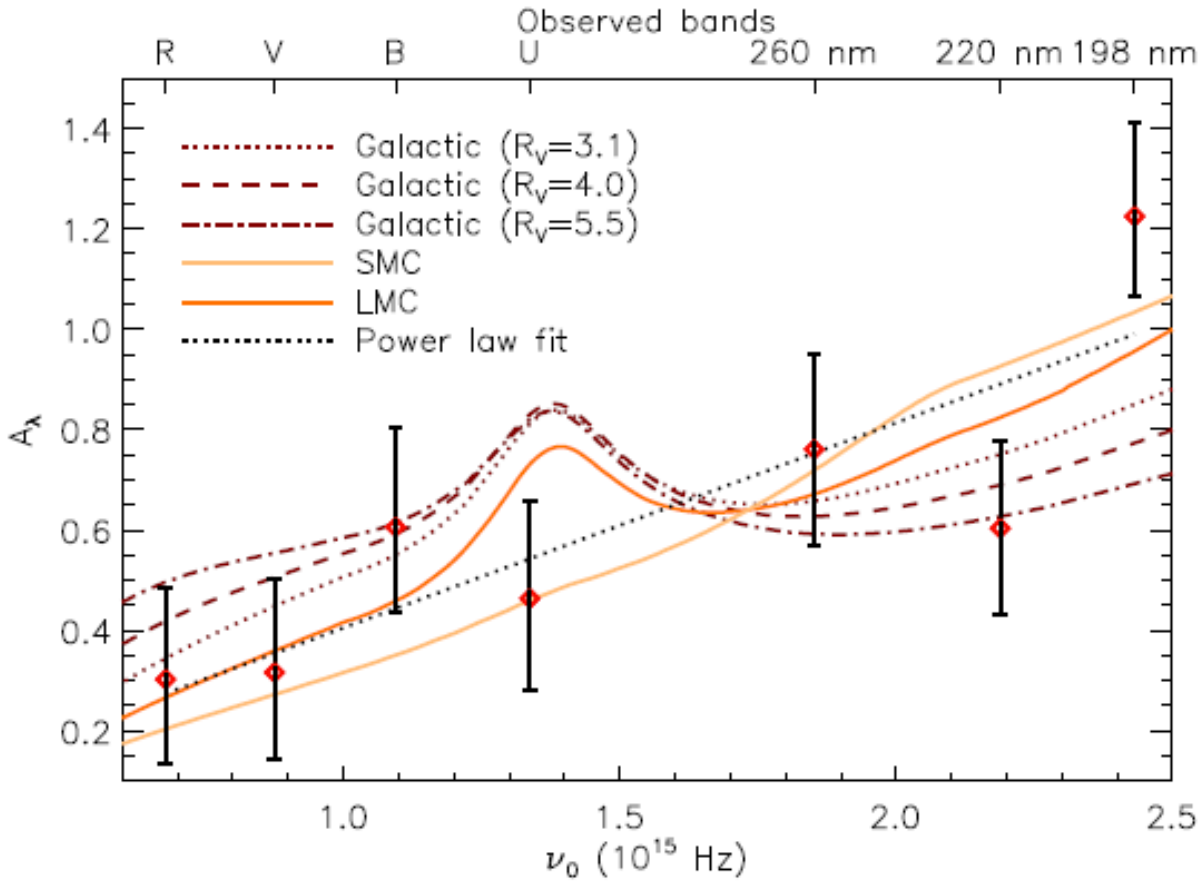

Fig. 2.— Measured extinction as a function of frequency for the Milky Way, the Large Magellanic Cloud, and the SMC. The bump is at about 2160 Å. Note the absence of the bump in the SMC curve (lowest metallicity of those shown), and the differences in overall index of the power law fits. This is Fig. 2 of Heng, Lazzati, Perna et al, 2008, a paper which attempts to demonstrate that extinction curves can be measured at high redshift using GRBs.

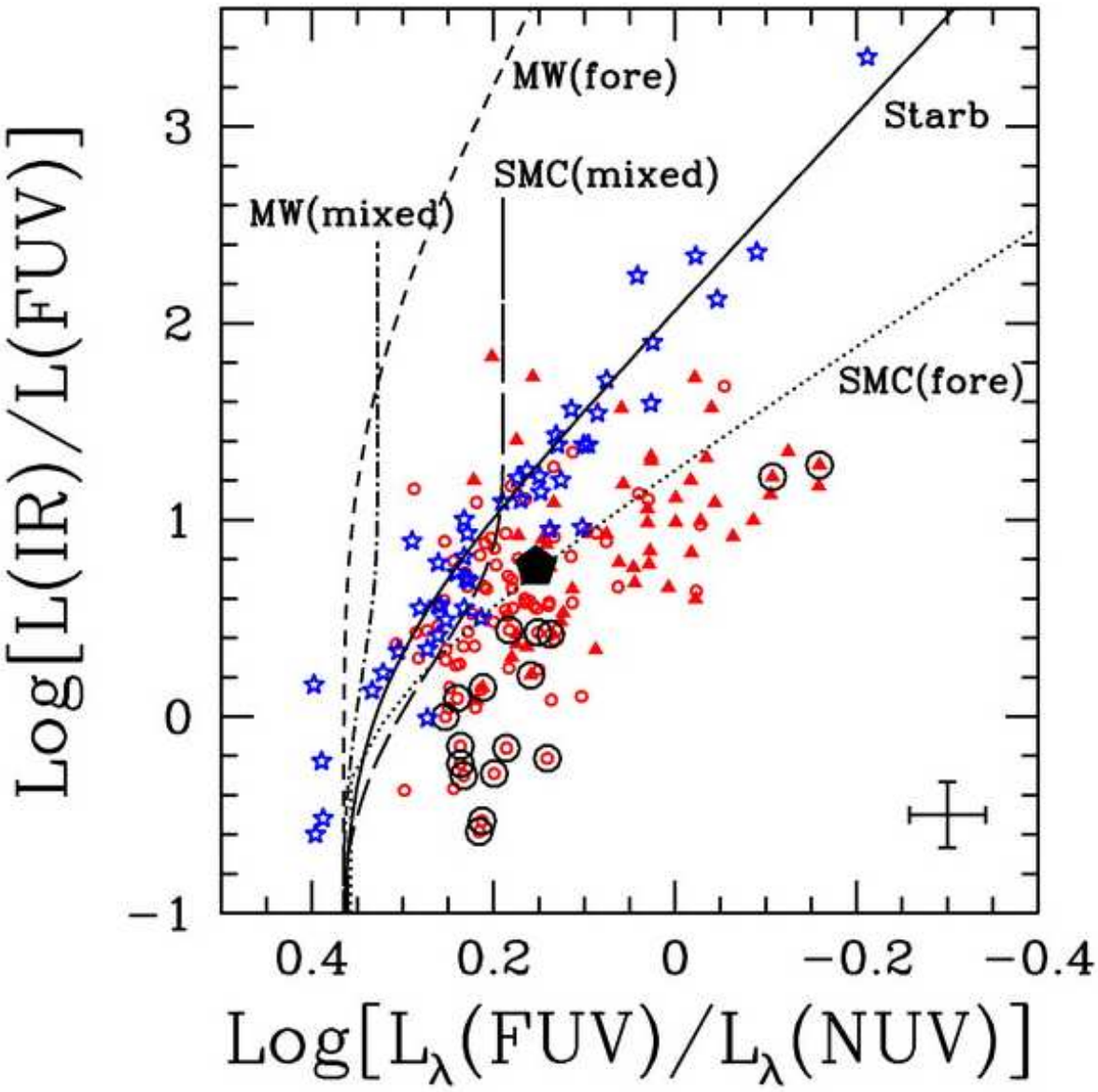

Fig. 3.— Total absorption, expressed as the ratio of IR-to-FUV luminosity as a function of the observed UV colors. Note the higher FUV/NUV luminosity increases to the left along the X axis. Data from 29 starburst galaxies from Calzetti et al (1994) are shown as open stars. Model lines are obtained by convolving the SED of a constant SFR population with a range of dust attenuation values and geometries: forground, non-scattering dust screens (Milky Way extinction curve: short dashed line, SMC extinction: dotted line), homogenous mixtures of stars and dust (MW ext. curve: dot-dashed line, SMC ext. curve: long dahsed line), and the starburst dust distribution (solid line). (Fig. 9 of Calzetti et al, 2005, ApJ, 633, 871)

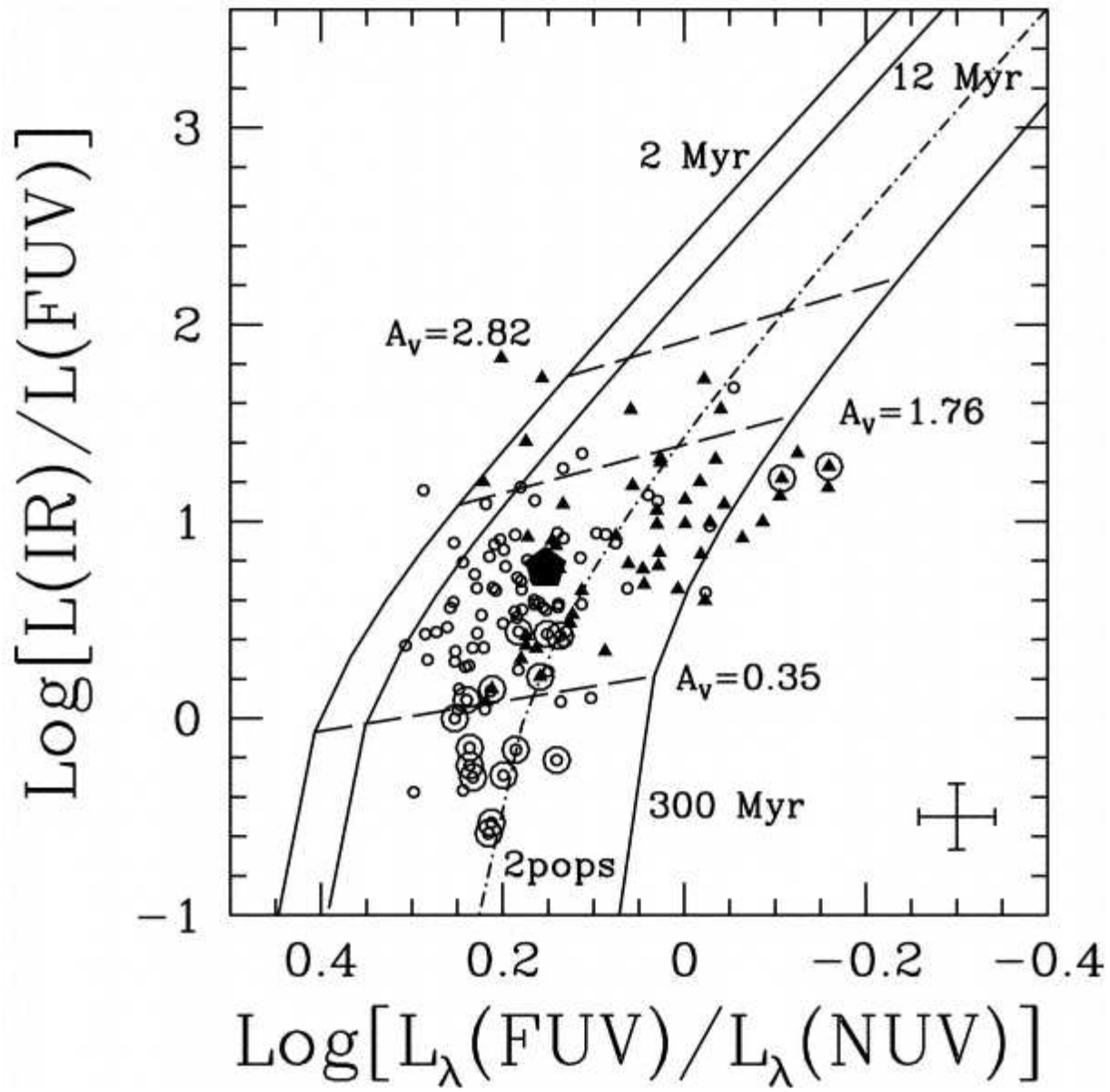

Fig. 4.— Same as above but now comparing to models of aging single burst populations convolved with the starburst absorption curve for increasing amounts of dust attenuation. Ages of 2, 12, and 300 Myr from the single burst are shown. The combination of a 5 Myr and a 300 Myr old single burst is shown as "2pops", with a mass ratio of 1/300 and a slightly higher extiction for the younger burst. Loci of constant extinction are marked by inclined dashed lines. The data are HII-emitting knots in the nearby spiral galaxy NGC 5194 (M51). Dust extinction at the center of M51 is 3.5 mag (a factor of 25) at 5000 Å. (Fig. 10 of Calzetti et al, 2005, ApJ, 633, 871)

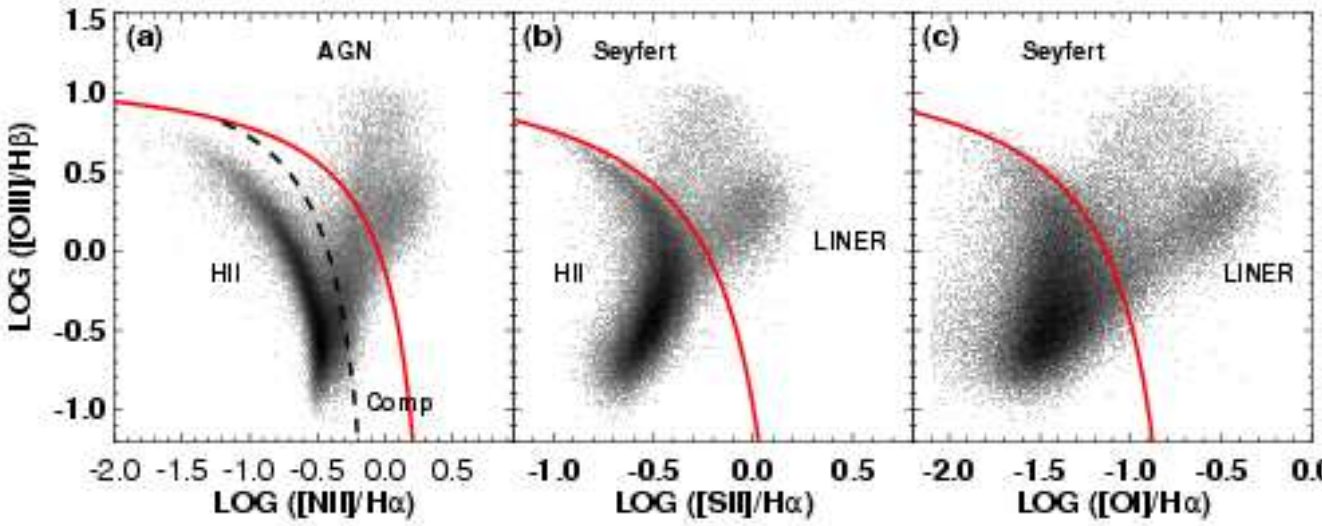

Figure 1. (a) The [N II]/Hα vs [O III]/Hβ diagnostic diagram for SDSS galaxies with S/N > 3. The Kewl (2001a) extreme starburst line and the Kauffmann et al. (2003a) classification line are shown as solid and dash respectively. (b) The [S II]/Hα vs [O III]/Hβ diagnostic diagram, (c) The [O I]/Hα vs [O III]/Hβ diagnostic diag

Fig. 5.— The curve defined by Lisa Kewyley and collaborators separating extreme starbursts is shown as a solid line; the Kauffmann et al classification line is shown as a dotted curve. (Fig. 1 of Kewley, Groves, Kauffman & Heckman 2006, MNRAS, 372, 961).

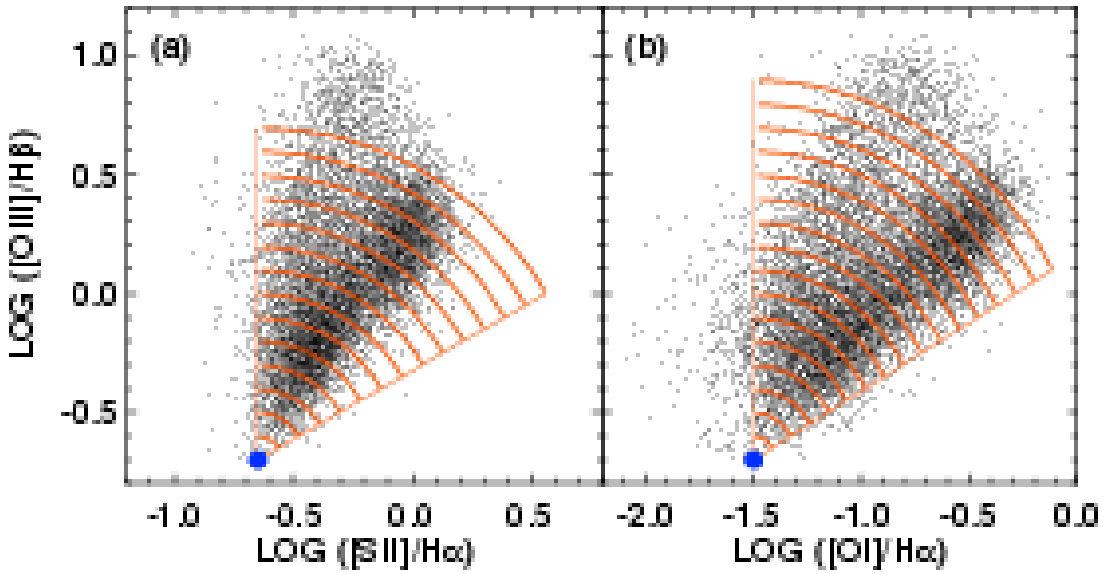

Figure 2. (a) The [S II]/Hα vs [O III]/Hβ and (b) [O I]/Hα vs [O III]/Hβ (right) diagnostic diagrams for SDSS galaxies classified as AGN using the Kauffmann et al. (2003a) line (dashed line in Figure 1a. The large filled circle represents the empirical base point p for the Seyfert and LINER sequences. Concentric arcs of 0.1 dex (red solid lines) show the binning of our sample with radius. We calculate histograms of angle from the x-axis centered at p for each bin.

Fig. 6.— Fig. 2 of Kewley, Groves, Kauffman & Heckman 2006, MNRAS, 372, 961).

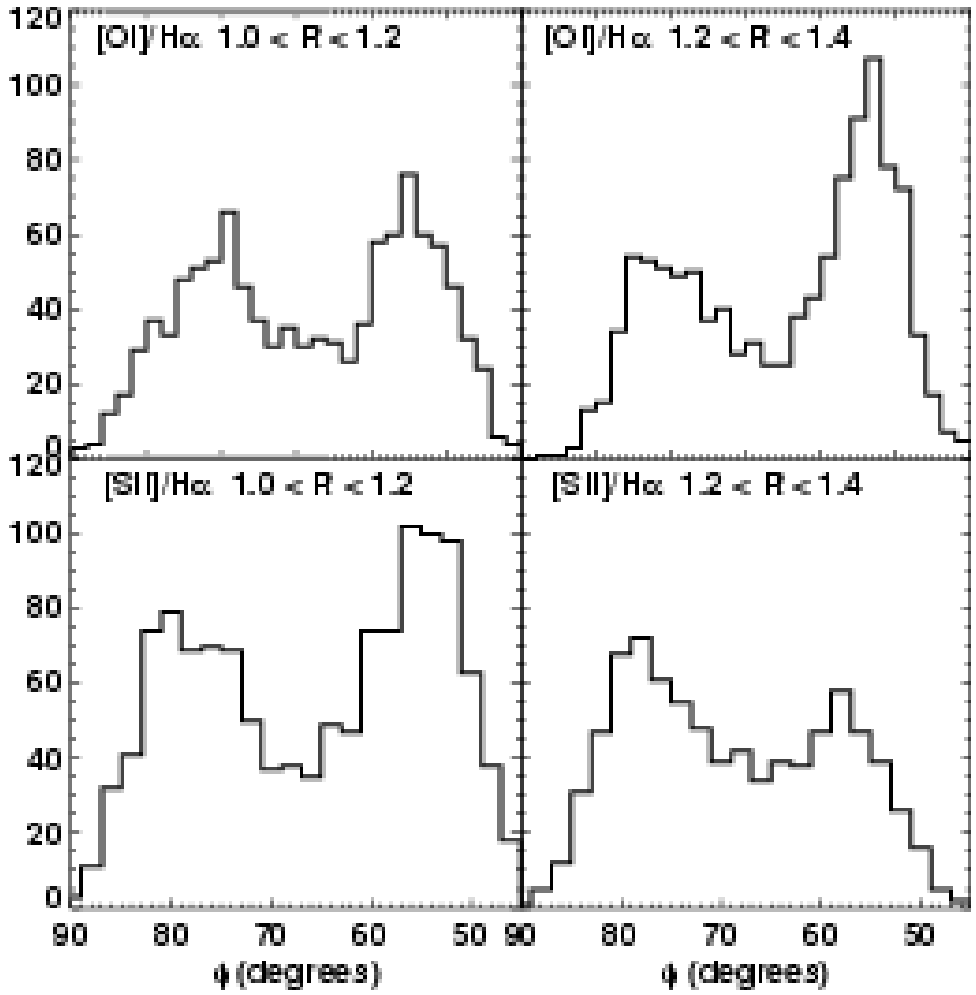

Figure 3. Histograms of the Seyfert and LINER sequences between 1.0-1.2 dex (left) and 1.2-1.4 dex (right) for the [O I]/Hα (top) and [S II]/Hα (bottom) diagnostic diagrams. The distribution is clearly bimodal. The LINER sequence is the right-hand peak and the Seyfert sequence is the left-hand peak.

Fig. 7.— Fig. 3 of Kewley, Groves, Kauffman & Heckman 2006, MNRAS, 372, 961).

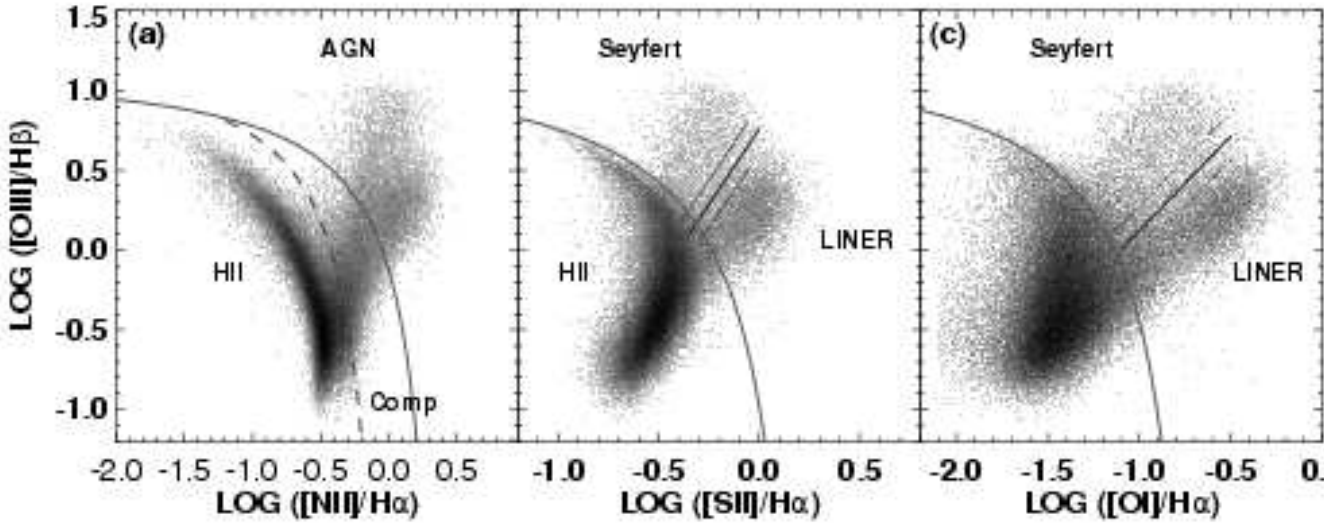

Figure 4. The three BPT diagrams showing our new scheme for classifying galaxies using emission-line ra
Kewley et al. (2001a) extreme starburst classification line (red solid), the Kauffmann et al. (2003a) pure star-f
line (blue dashed), and our new Seyfert-LINER line (blue solid) are used to separate galaxies into H II re
Seyferts, LINERs, and Composite H II-AGN types.

Fig. 8.— Fig. 4 of Kewley, Groves, Kauffman & Heckman 2006, MNRAS, 372, 961).

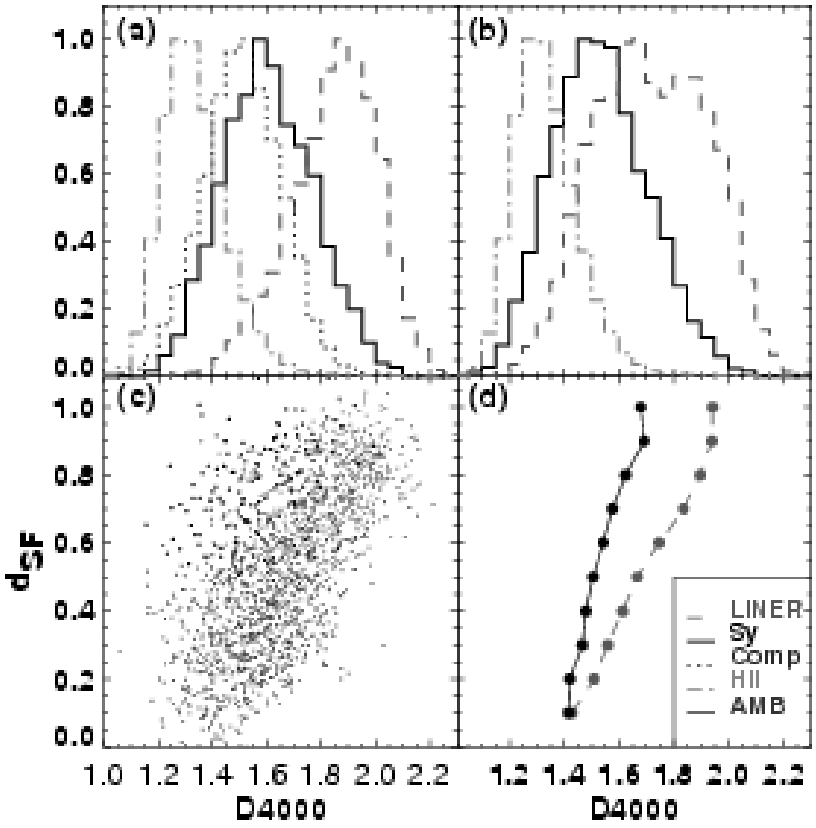

Figure 11. (a) The distribution of D4000 for LINERs (red dashed), Seyferts (black solid), composites (blue dotted) and H II region-like galaxies (green dot-dashed). (b) The distribution of D4000 for LINERs (red-dashed), Seyferts (black solid), and H II region-like galaxies (green dot-dashed) where LINERs and Seyferts include LINER+H II and Seyfert+H II composites. Only pure star-forming galaxies classified according to the Ka03 classification line (equation 1) and LINER/Seyfert ambiguous galaxies are excluded. (c) D4000 for a uniform random sampling of the Seyferts (black) and LINERs (red), composites (blue) and ambiguous galaxies (purple) as a function of distance from the Ke01 line. (d) The median D4000 for Seyferts (black) and LINERs (red) as a function of distance from the Ke01 line, including Seyfert+H II and LINER+H II galaxies. A distance of 1.0 indicates that the optical line ratios are dominated by ionizing radiation from the Seyfert or LINER nucleus.

Fig. 9.— Fig. 11 of Kewley, Groves, Kauffman & Heckman 2006, MNRAS, 372, 961).

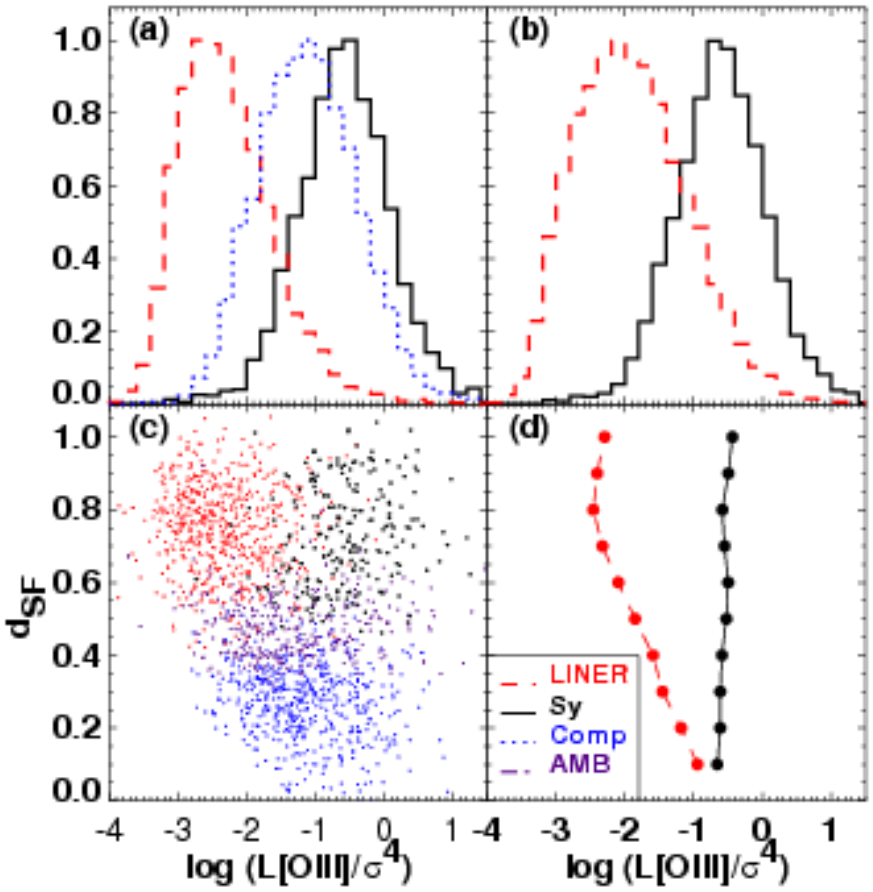

Figure 20. (a) The distribution of the logarithm of L[OIII]/σ^4 (corrected for extinction) for LINERs (red dashed), Seyferts (black solid), composites (blue dotted) and H II region-like galaxies (green dot-dashed). (b) The distribution of L[OIII]/σ^4 for LINERs (red-dashed), Seyferts (black solid), and H II region-like galaxies (green dot-dashed) where LINERs and Seyferts include LINER+H II and Seyfert+H II composites. (c) L[OIII]/σ^4 for Seyferts (black) and LINERs (red), composites (blue) and ambiguous galaxies (purple) as a function of distance from the Ke01 line. (d) L[OIII]/σ^4 for Seyferts (black) and LINERs (red) as a function of distance from the Ke01 line, including Seyfert+H II and LINER+H II galaxies. A distance of 1.0 indicates that the optical line ratios are dominated by ionizing radiation from the Seyfert or LINER nucleus.

Fig. 10.— Fig. 20 of Kewley, Groves, Kauffman & Heckman 2006, MNRAS, 372, 961).

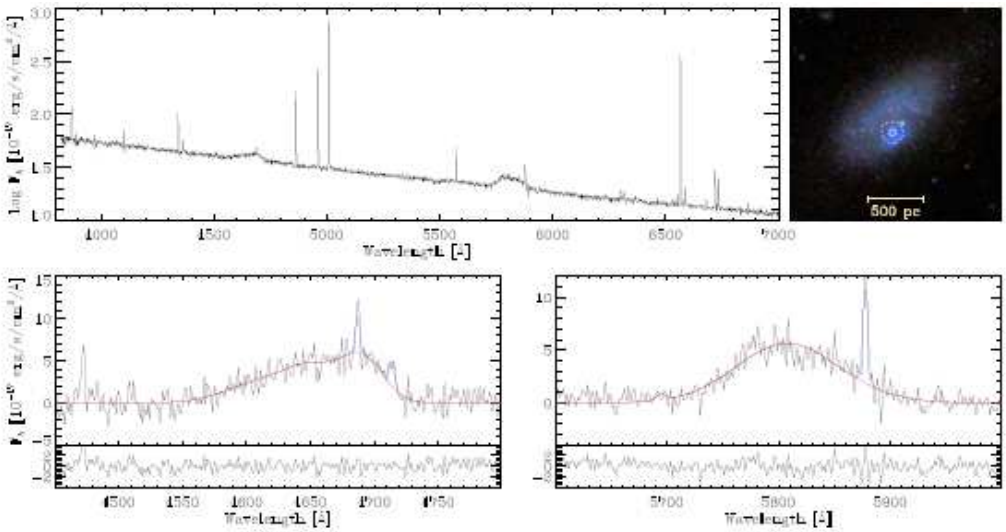

Fig. 21. Top row: On the left, the rest-frame SDSS spectrum of Mrk 178 in units of log F_λ, the blue and red bump are both very prominent, note also the relatively weak emission lines. On the right a colour image of Mrk 178 from the SDSS with the location of spectroscopic observations indicated by the circles. The outer, dashed, circle is 10" in diameter while the inner circle shows the size of the SDSS fibre, 3" in diameter. The bottom row shows the continuum subtracted spectra around the blue bump, on the left, and the red bump on the right, with the residuals after subtracting the fit to the nebular and WR lines indicated in the panel below each as in Figure 2.

Fig. 11.— Fig. 21 of Brinchmann, Kunth & Durret, 2009, A&A)

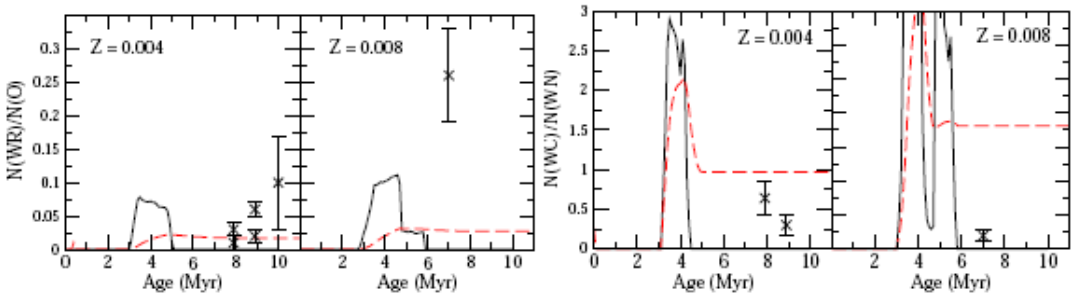

Figure 7. Left panels: time evolution of the ratio of WR to O stars according to Starburst99 predictions. Right panel: same but for the ratio of WC to WN stars. In both cases, results for two metallicities, Z= 0.004 and Z=0.008, are shown. Solid lines represent instantaneous star formation models and dashed line continuous star formation ones. Crosses represent the derived numbers for each galaxy taking into account the measured luminosities of the bumps as compared with those predicted by the Starburst99 models at the predicted age. The number of O stars has been derived using the same procedure for L(Hα).

Fig. 12.— Fig. 7 of Perez-Montero, Garcia-Benito, Hagele & Diaz, 2010, MNRAS, in press Astro-ph 1001.4828)

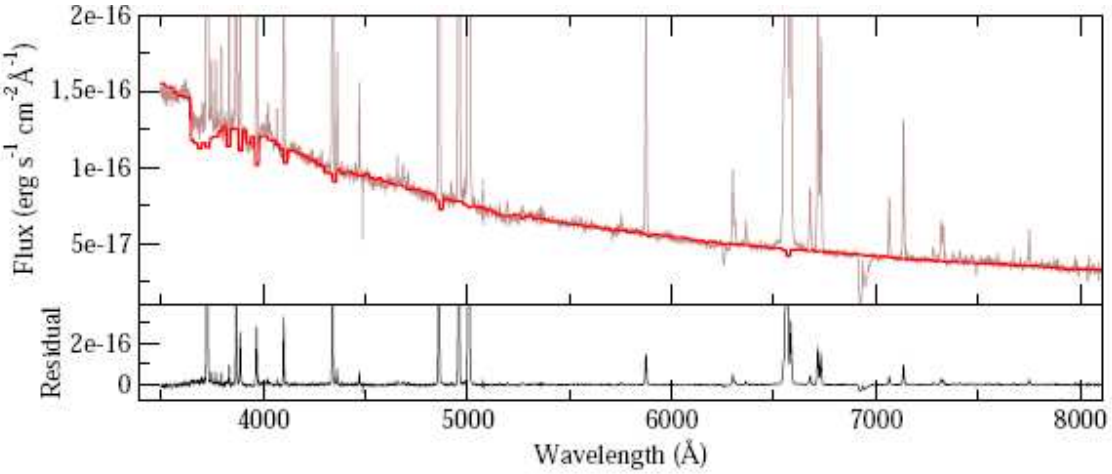

Figure 1. In the solid brown line, optical spectrum of the galaxy J0021 and comparison with the spectral fitting carried out with the code STARLIGHT, using spectral libraries from Starburst99, represented by the solid red line. In the lower panel, we show the residuals of the fit, which represents the nebular spectrum.

Fig. 13.— Fig. 1 of Perez-Montero, Garcia-Benito, Hagele & Diaz, 2010, MNRAS, in press Astro-ph 1001.4828)

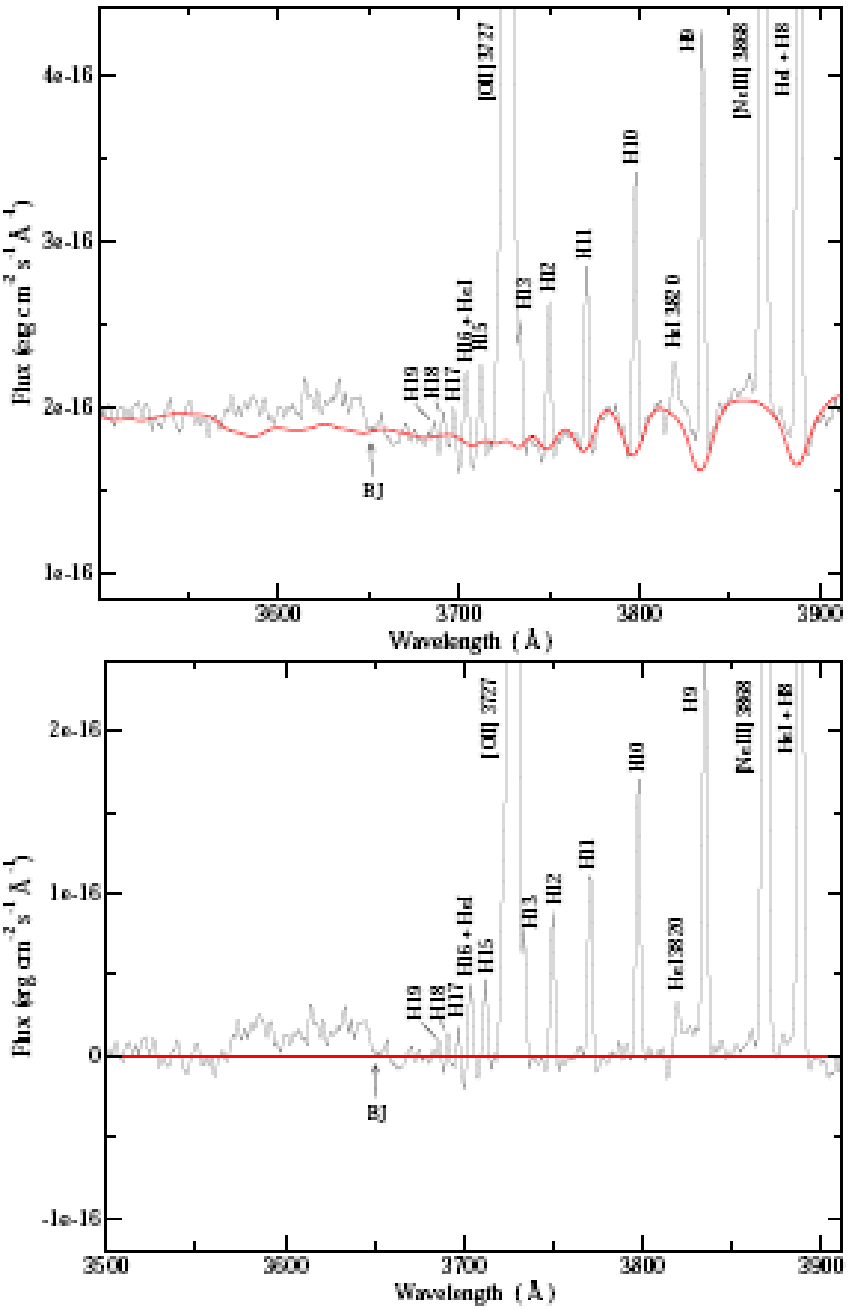

Figure 2. Upper panel, in black, optical spectrum of the galaxy J1624 in the spectral range 3500 - 3912 Å, around the Balmer jump and the high order Balmer series, together with the fitting (red line) performed using the STARLIGHT spectral synthesis code. Lower panel, subtraction of this fitting from the WHT spectrum in the same spectral range; the solid red line shows the zero level.

Fig. 14.— Fig. 2 of Perez-Montero, Garcia-Benito, Hagele & Diaz, 2010, MNRAS, in press Astro-ph 1001.4828)

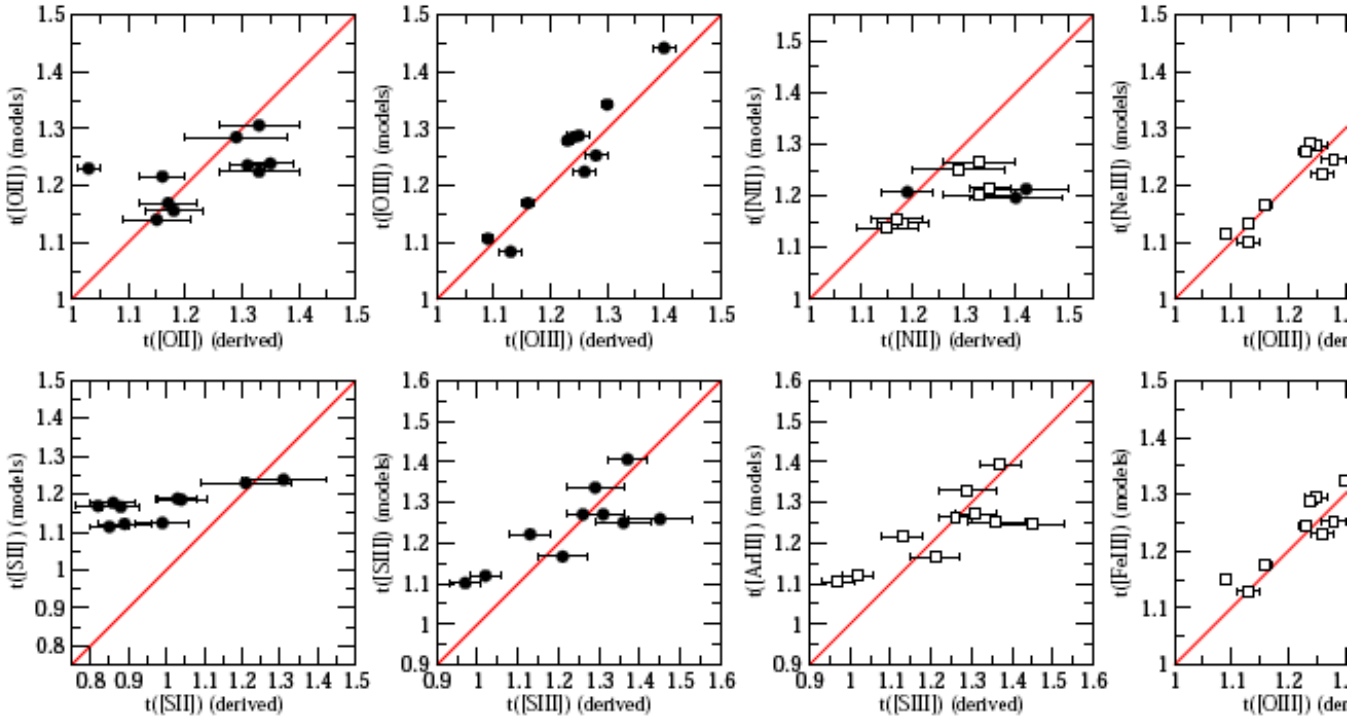

Figure 8. Comparison between the electron temperatures (in units of 10^4 K) as derived from the observations and fr
made photoionization models. Black circles represent a comparison between a temperature directly derived in the
while white squares represent a temperature of another ion, assumed to be similar in the thermal structure.

Fig. 15.— Fig. 8 of Perez-Montero, Garcia-Benito, Hagele & Diaz, 2010, MNRAS, in press Astro-ph 1001.4828)

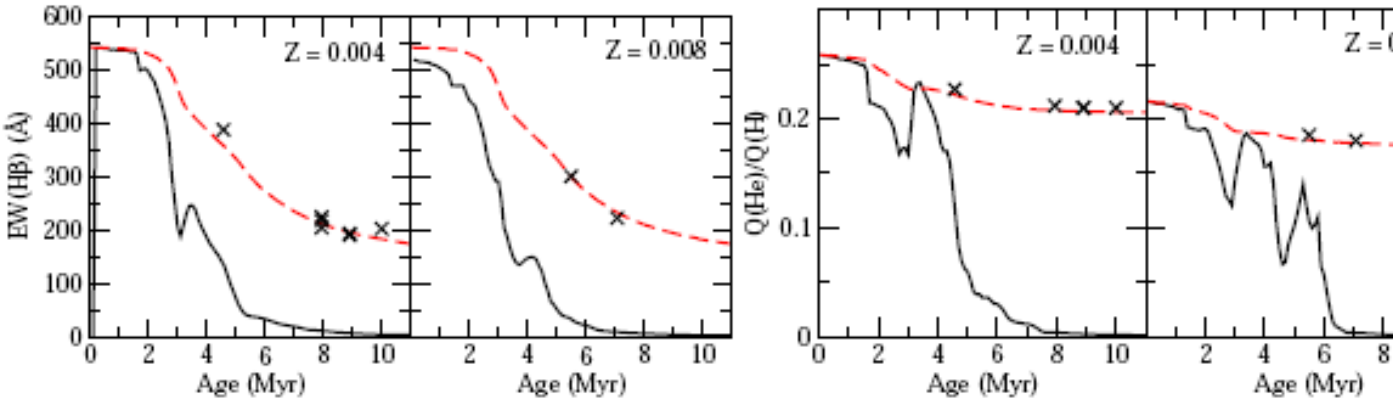

Figure 5. Left panels: relation between the equivalent width of Hβ and the age of the corresponding synthesis population for metallicities of 0.004 and 0.008 as predicted by Starburst99. Crosses represent the observed values measured on the stellar continua and multiplied by the corresponding absorption factor obtained in each tailor-made model. The assigned each object is that predicted by the same models. Therefore, the J1540 point does not appear as the fitted age is older than 1 Right panels: relation between the ratio of helium to hydrogen ionizing photons and the age of the ionizing cluster. In all the black solid line represents an instantaneous star formation and the red dashed line, a continuous star formation as pre by Starburst99. As in the previous case, crosses represent the values obtained from the models for each object, with the exc of J1540.

Fig. 16.— Fig. 5 of Perez-Montero, Garcia-Benito, Hagele & Diaz, 2010, MNRAS, in press Astro-ph 1001.4828)

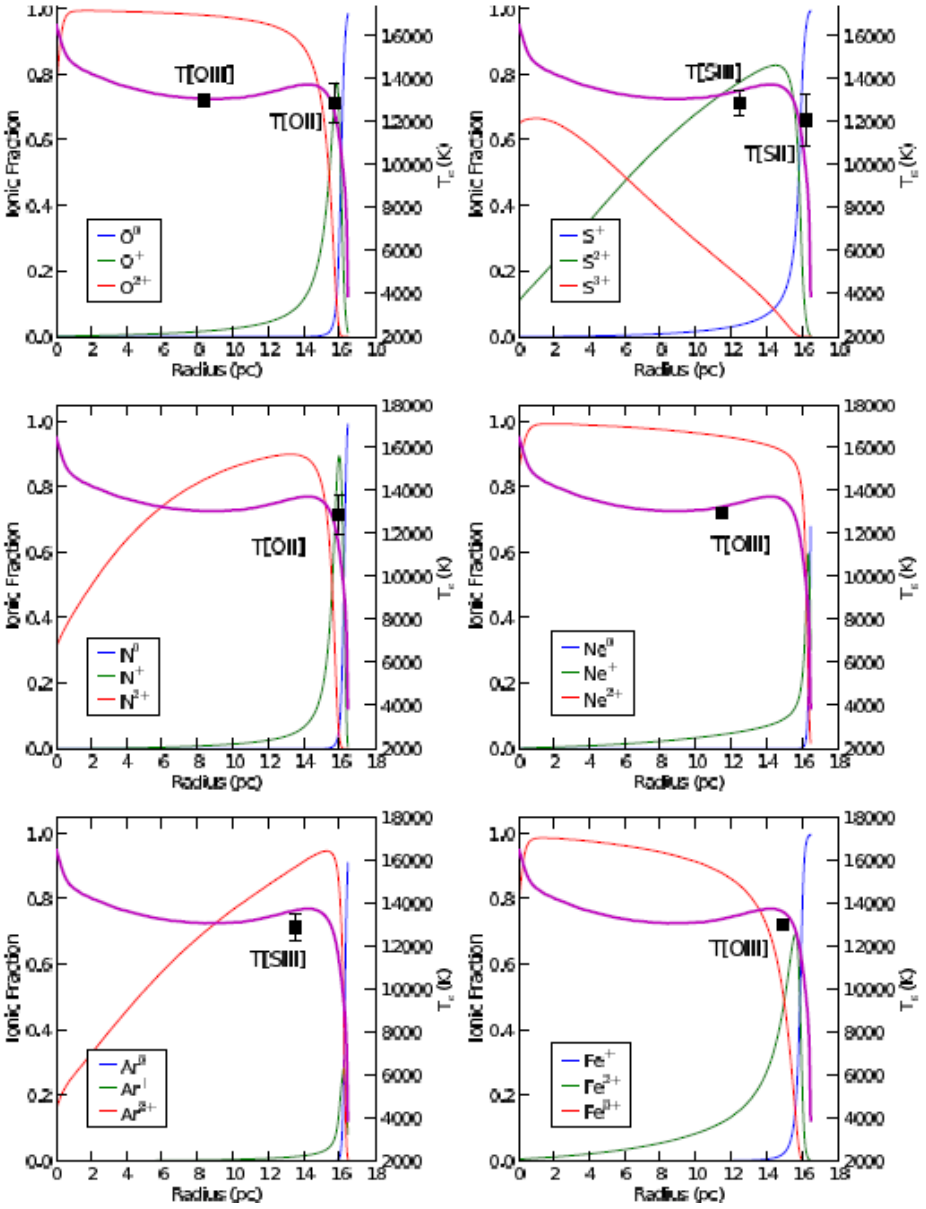

Fig. 17.— Radial profile of T_e (right vertical axis, thick violet line) and relative abundance of various ionic species (left vertical axis, thin solid curves) as calculated in the best photoionization "tailor-made" model of the galaxy J1616. The derived T_e are shown as black squares in the position of the average abundance of the corresponding ions. (Fig. 9 of Perez-Montero, Garcia-Benito, Hagele & Diaz, 2010, MNRAS, in press Astro-ph 1001.4828)

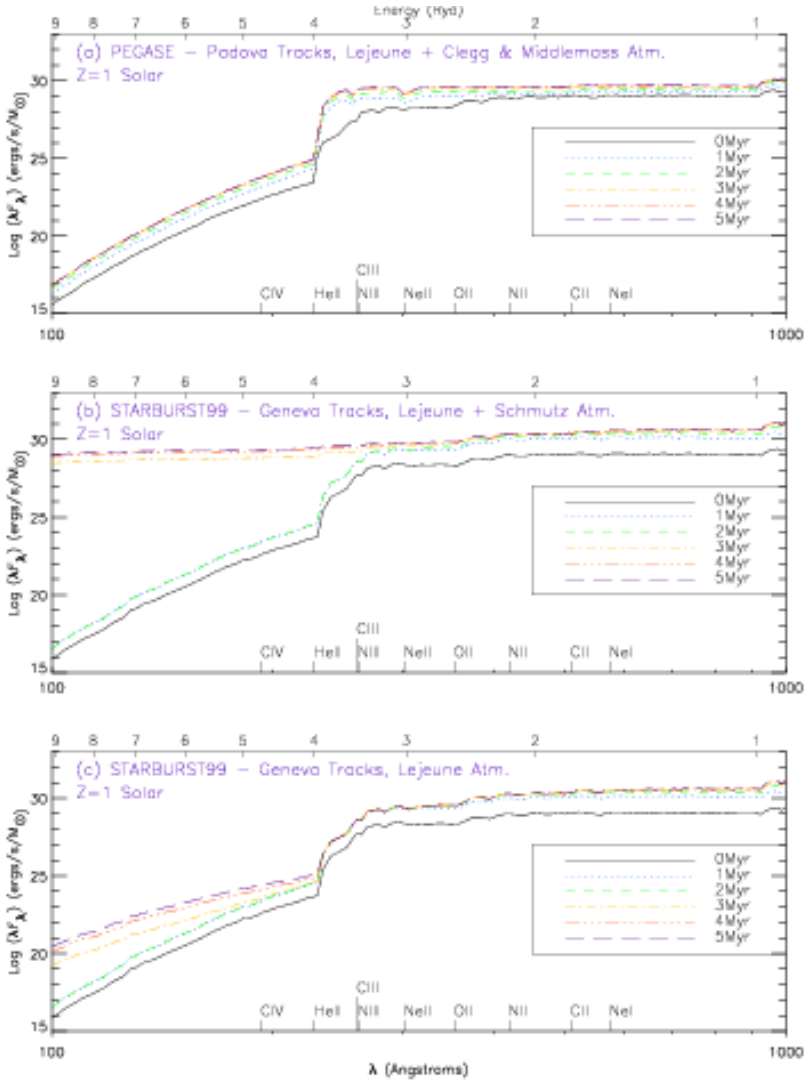

Fig. 1.— The ionizing spectral energy distribution (normalised to the flux at the Lyman limit) as a function of age of the starburst for (a)the PEGASE models, (b) and the Lejeune plus Schmutz atmospheres and (c) the STARBURST99 models for Lejeune atmospheres. Ionization edges are shown for some elements. Note the rapid intitial evolution as the Wolf-Rayet stars evolve, and the convergence toward an asymptotic solution when a stochastic balance between star births and star deaths is achieved for all masses which contribute to the EUV continuum. All models produce very similar results at zero age, but differ markedly at later times, mainly reflecting differences between the extended stellar atmosphere models used (Clegg & Middlemass (1987) for PEGASE

Fig. 18.— Fig. 1 of Kewley, Dopita, Sutherland et al (2001, ApJ, 556, 121).

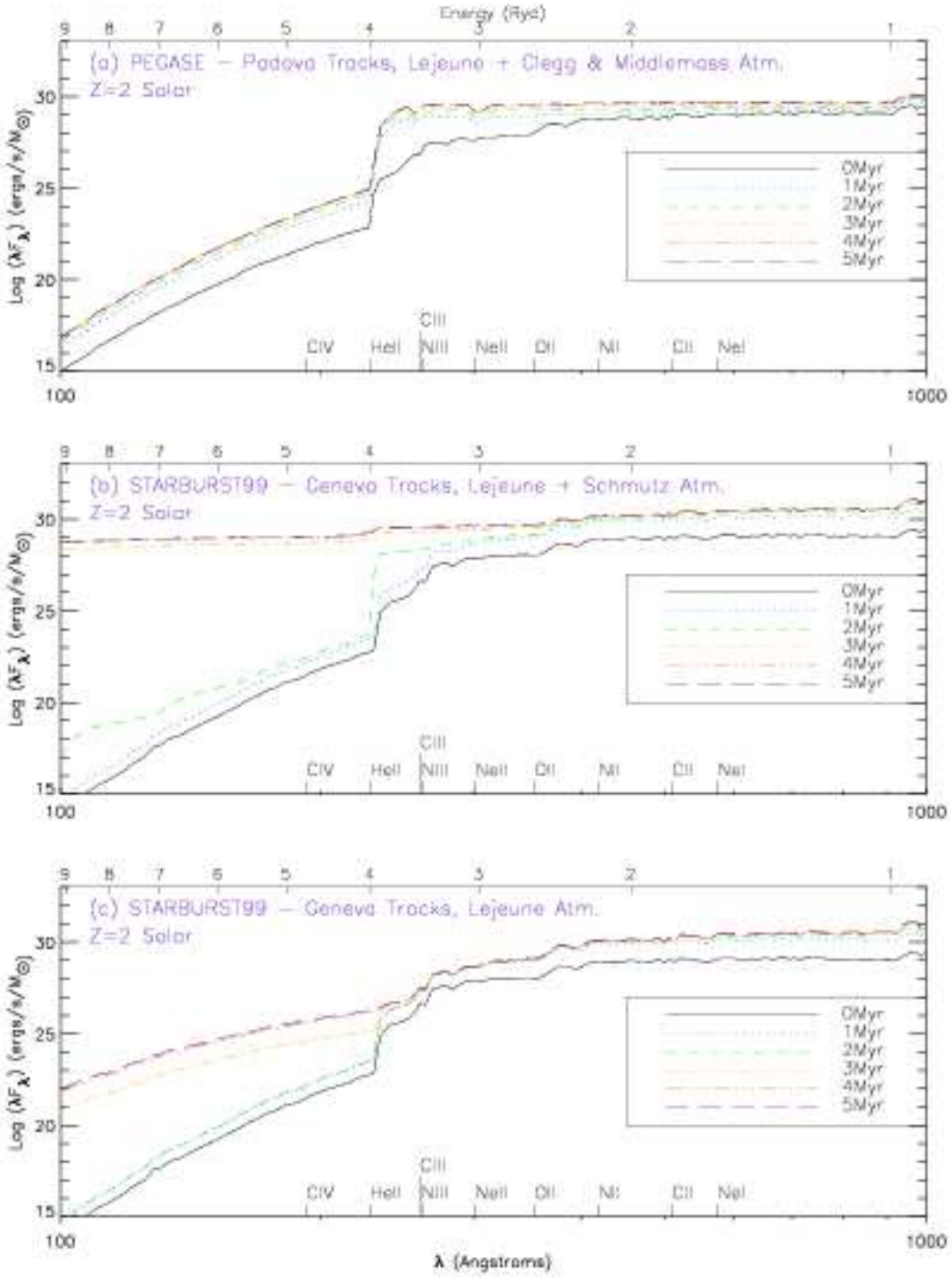

Fig. 3.— As in Figure 1, except Z=2 × solar metallicity.

Fig. 19.— Fig. 3 of Kewley, Dopita, Sutherland et al (2001, ApJ, 556, 121). Same as fig.1 but for twice solar metallicity.

To determine the ionization levels of the various elements, one needs to know the electron temperature. The strength of forbidden lines is easy to calculate since they are almost always optically thin in HII regions and the density is low, so collisional de-excitation can be ignored. This results in an overpopulation of the metastable states and the forbidden transitions dominate the spectrum. If one can find a single ion with two or more detectable forbidden lines arising from very different excitation energy levels, the ratio of their strengths will yields a measure of temperature. The key diagnostic lines used include 4363 Å of [OIII], but this line is often too weak to be observed. Note that these are all forbidden lines, which means they have low transition probabilities.

When the 4363 Å line is too weak to be detected, one can use strong-line ratios as first laid out by Pagel et al (1979). $R_{23} = ([OII]3727 + [OIII]4959, 5007)/H\beta$ is the most common such ratio. The problem is that R_{23} is not monotonic with [Fe/H]; it is double valued with metallicity, having a "lower branch" and a high estimate for most values of R_{23}. This degeneracy can be broken by adding other line ratios such as [NII]/[OII], but the [NII] lines are often weaker and this ratio is badly affected by extinction due to the wide wavelength range between the two lines used.

Clumping within HII regions or presence of outer shells around HII regions can affect the deduced abundances.

All these diagnostics were developed for HII regions and have been under development and use for decades. For $z > 1.2$ most of the relevant lines have shifted from the optical into the near-IR, where it is much harder to obtain the necessary data for these faint sources. Development of new metrics for high redshift galaxies was required.

HII galaxies, first described by Sargent & Searle (1970, ApJ, 162, L155), are compact dwarf galaxies which have intense bursts of recent star formation and their spectra are dominated by very bright emission lines. They are of low mass, and prior to HST there

was a controversy about whether they contained any old population at all, or were truly "young galaxies" just beginning to form stars. With the spatial resolution of HST, deep CMDs revealed the presence of an old population, and the "young galaxy" paradigm was abandoned.

Thesse low luminosity galaxies have no obvious chemical gradient and are metal-poor. IZw18 is the HII galaxy with lowest mean metal content for the ISM in the Local Universe (see, e.g. Searle & Sargent, 1972, ApJ, 173, 25).

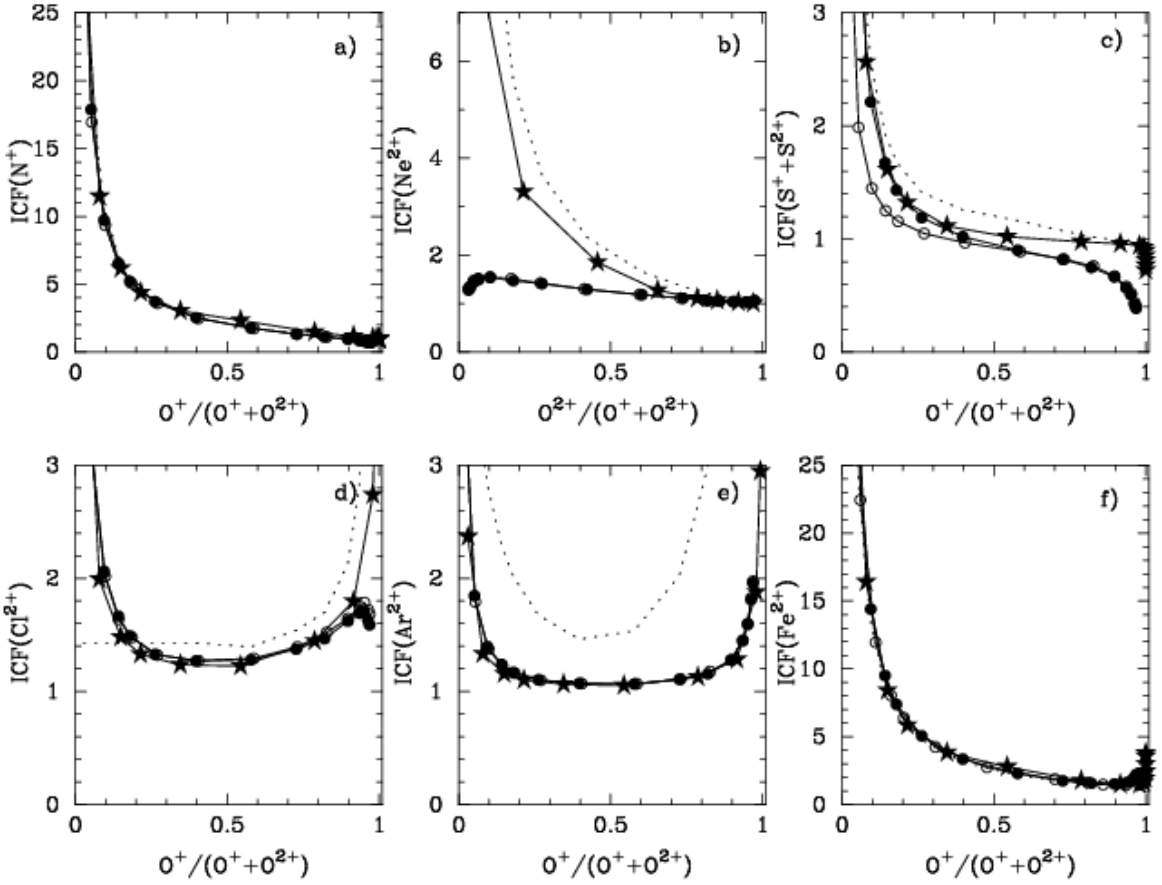

Fig. 9. Ionization correction factors for heavy elements. Filled circles are for the models with $Z = 0.02\ Z_{\odot}$, open circles are for the models with $Z = 0.05\ Z_{\odot}$, and stars are for the models with $Z = 0.2\ Z_{\odot}$. The dotted line is the approximation of the models of Stasińska (1990).

Fig. 20.— Fig. 9 of Izotov, Stasinska, Meynet, Guseva & Thuan, 20006, A&A, 448, 955.

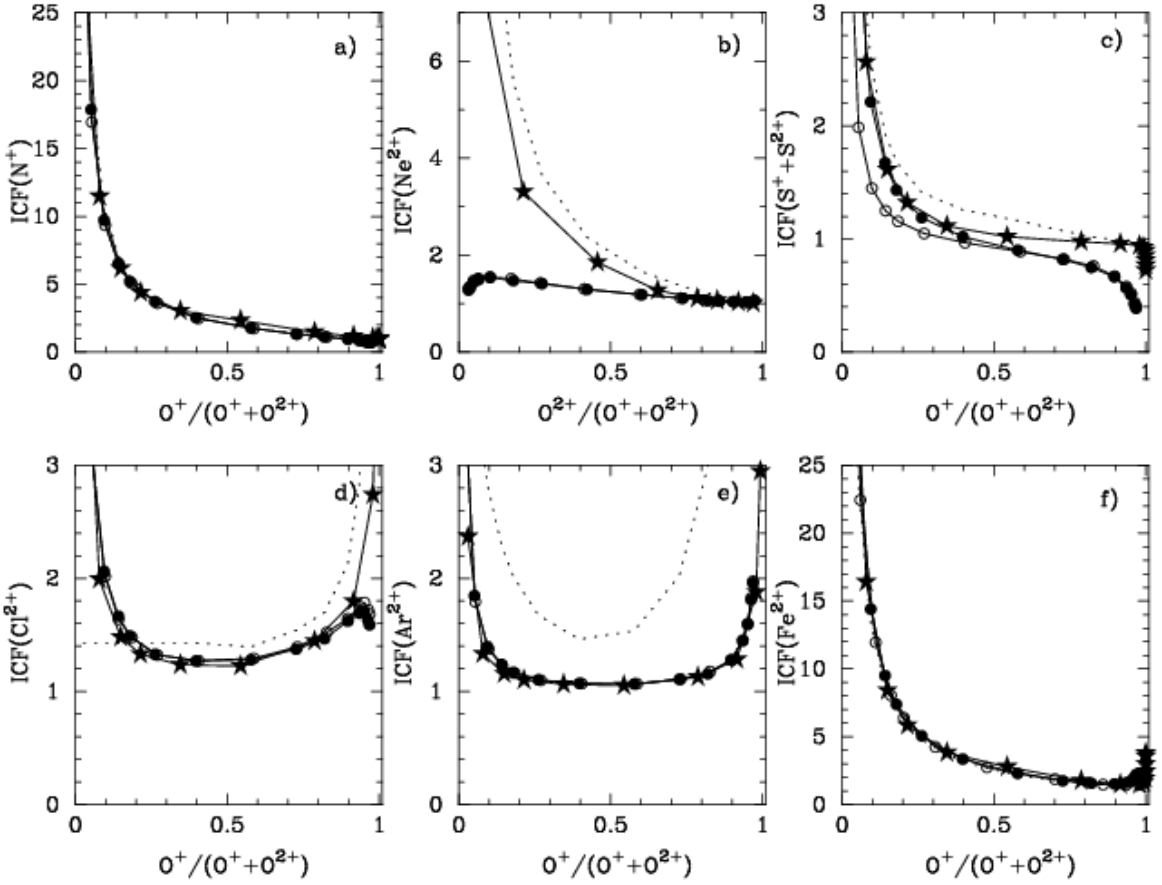

Fig. 9. Ionization correction factors for heavy elements. Filled circles are for the models with $Z = 0.02\ Z_{\odot}$, open circles are for the models with $Z = 0.05\ Z_{\odot}$, and stars are for the models with $Z = 0.2\ Z_{\odot}$. The dotted line is the approximation of the models of Stasińska (1990).

Fig. 21.— Fig. 11 of Izotov, Stasinska, Meynet, Guseva & Thuan, 20006, A&A, 448, 955.

1.3. Evidence for Clumpiness in the Gas

Measurements made in distant HII regions are of projected quantities through a column of the ISM. For example, we determine T_C, the column mean temperature, which is T_e integrated through the line of sight through the HII region, but not $T_e(x, y, z)$. A parameter to measure clumping is $t^2 = \int (T_c - T_0)^2 N_e N_i dV / T_0^2 \int N_e N_i dV$, where T_0 is the the volume mean T_0 is $T_e$integrated over $N_e N_i dV$) Nearby HII regions in the galaxy are well resolved spatially. There have been a number of studies of these, as t^2 can be measured from the small scale variations in the plane of the sky of the forbidden line strengths. O'Dell, Peimbert & Peimbert (2003, AJ, 125 2590) describe one such effort using WFPC2/HST images of the Orion nebulae taken through narrow-band interference filters. They have more than 1 million independent temperature measurements. They find that the measured t^2 for the Orion nebula is larger than that expected for uniform-density chemically-homogenous photoionization models. This is important as clumpiness significantly affects the derived abundances.

We present a high spatial resolution map of the columnar electron temperature (T_c) of a region to the south west of the Trapezium in the Orion Nebula. This map was derived from Hubble Space Telescope images that isolated the primary lines of H I for determination of the local extinction and of the [O III] lines for determination of T_c. Although there is no statistically significant variation of T_c with distance from the dominant ionizing star θ^1 Ori C, we find small scale variations in the plane of the sky down to a few arcseconds that are compatible with the variations inferred from comparing the value of T_e derived from forbidden and recombination lines, commonly known as the t^2 problem. We present other evidence for fine scale variations in conditions in the nebula, these being variations in the surface brightness of the the nebula, fluctuations in radial velocities, and ionization changes. From our T_c map and other considerations we estimate that $t^2 = 0.028 \pm 0.006$ for the Orion nebula. Shadowed regions behind clumps close to the ionization front can make a significant contribution to the observed temperature fluctuations, but they cannot account for the t^2 values inferred from several methods of temperature determination. It is shown that an anomalous broadening of nebular emission lines appears to have the same sense of correlation as the temperature anomalies, although a causal link is not obvious.

Fig. 22.— Abstract of paper by O'Dell, Peimbert & Peimbert (2003, AJ, 125 2590) on clumpiness of HII regions.

1.4. Planetary Nebulae

A PN consists of material ejected with a modest velocity from an evolved star; the material appears as a shell around the star which is resolved for the nearer objects. The central star is very hot, with T_{eff} approaching 100,000 K. This means that the gas is highly ionized, much more so than in an HII region, where the ionizing field comes from many stars which may be quite far away from the gas in the mean compared to the distance a PN shell is from its central star, which is about 3×10^{17} cm. Thus PN emission lines arise from highly ionized species such as HeII and OIII. Since only a single star ionizes a PN, the strength of its emission lines is much less than that of a HII region, which presumably contains a young stellar cluster with many very luminous massive stars. So the study of PN is restricted to relatively nearby galaxies.

Mid-IR spectra are very useful for studying PN abundances, as the transition involves only a small change in energy of the lower and upper state, and hence the level populations are less depenedent on temperature. Furthermore, there are more suitable pairs of lines for determining T_e in the mid-IR spectra of PN than in the optical. Of course the ionization correction factors converting between abundance of a particular species into that of the element are still important and must be calculated.

Pottasch and Salas (2010, arXiv:1005.3042) have pursued this, and obtained reasonably accurate abundances of several key elements for many Galactic PN, including H, He, C, N, O by combining analysis of optical and mid-IR spectra. They then compare the resulting abundance ratios in PN with production yields for AGB stars of various mass to try to deduce the initial mass of the PN central star and verify the consistency of the calculated production yields for AGB stars. (They use the calculated yields of Karakas.)

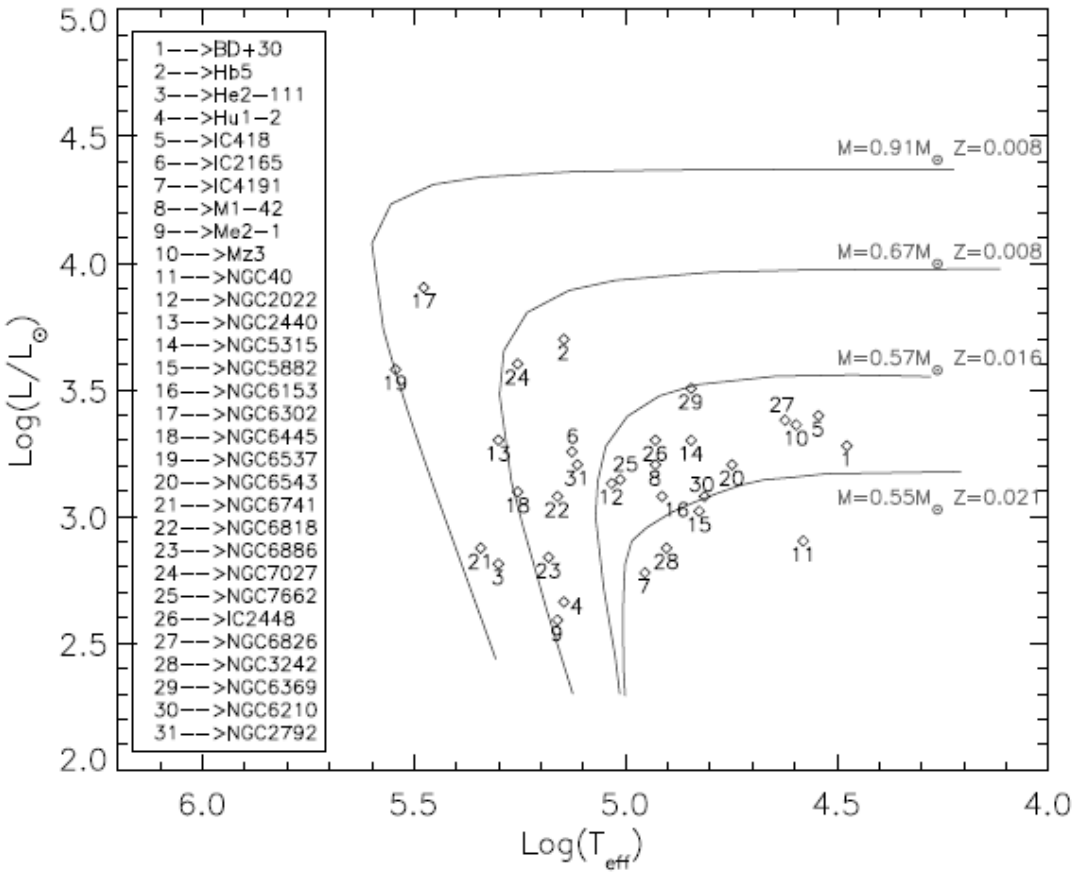

Fig. 4. The HR diagram. The models for core masses of 0.57, 0.67 and 0.91$M_\odot$ are taken from Vassiliadis & Wood(1993) while the 0.55$M_\odot$ model is from Schönberner(1983).

Fig. 23.— A CMD with evolutionary tracks for PNs. Note the high T_{eff}, ranging up to 300,000 K, the small range in mass, and the high luminosity (up to 20,000 $L_\odot$. (Fig. 4 of Pottasch & Bernard-Salas 2010).

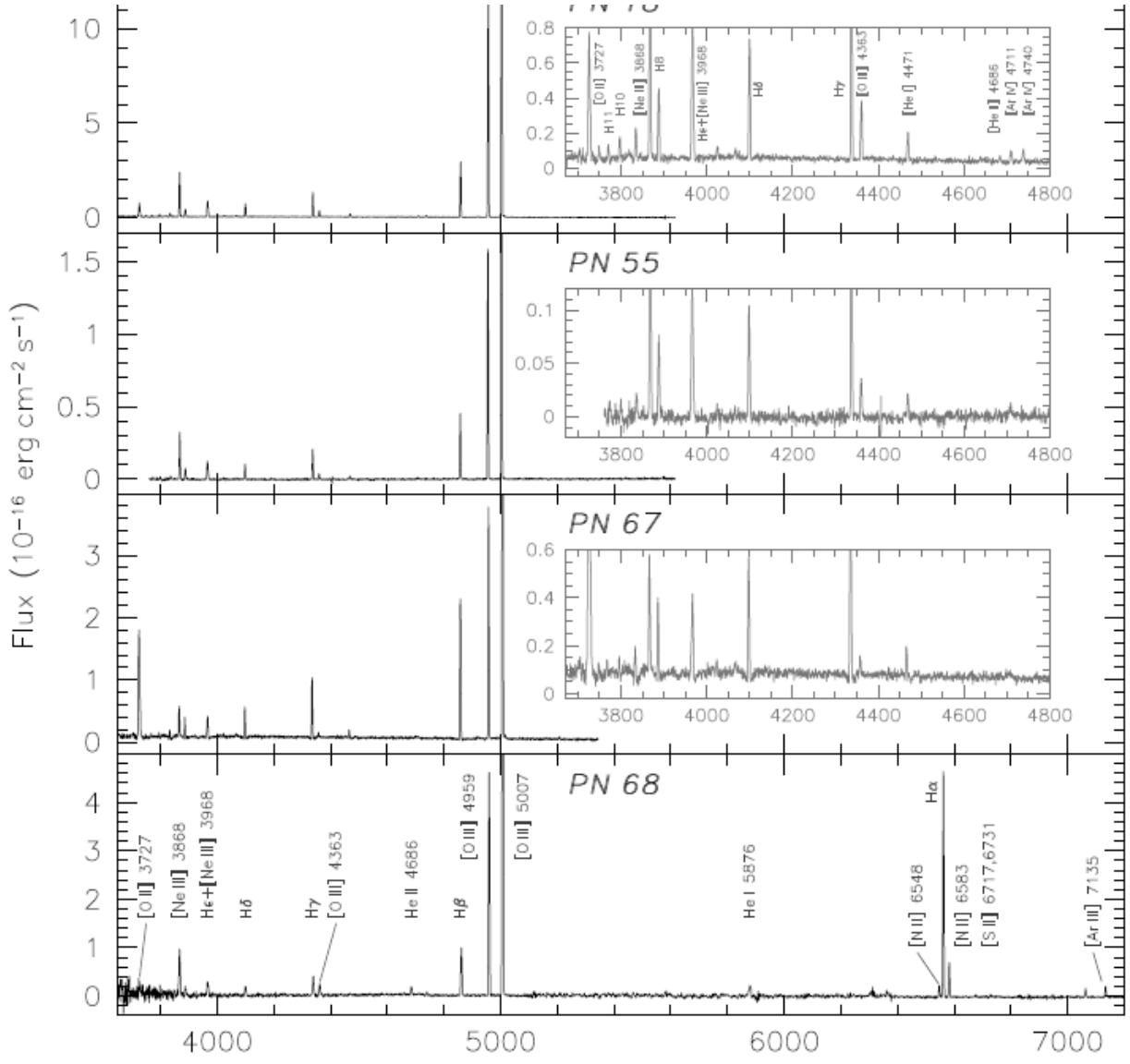

Fig. 24.— The optical spectra of some PN in the nearby spiral galaxy M33. Zoomed in views are provided in the inserts to better display the weakest features, and the main emission lines are identified in the bottom spectrum. This is Fig. 1 of Bresolin et al (2010).

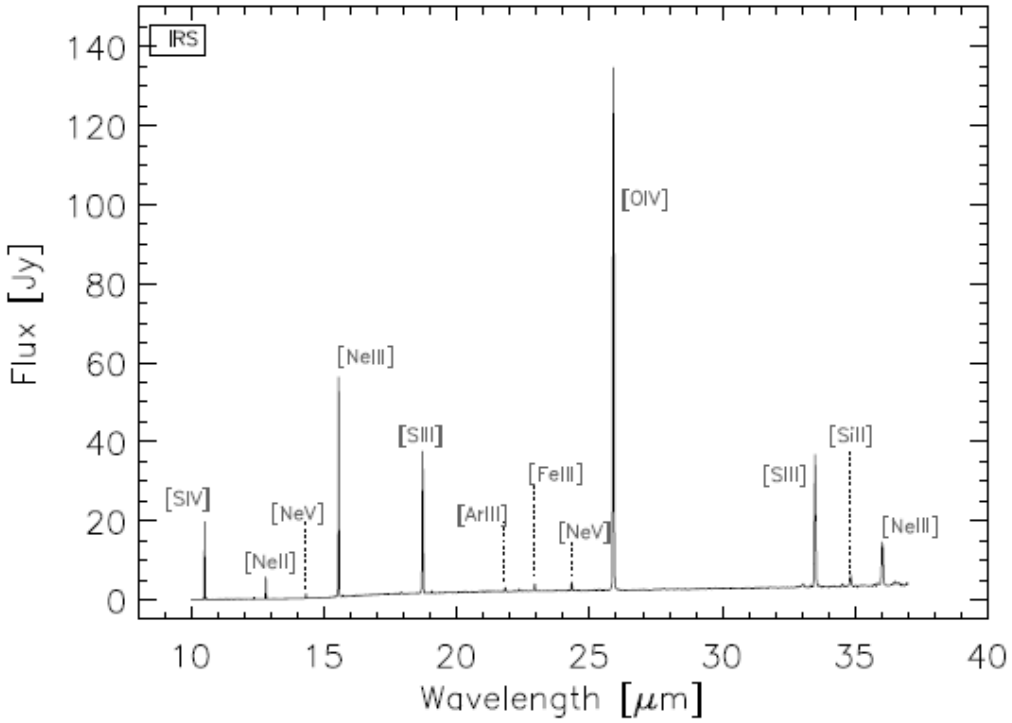

Fig. 2. Observed Spitzer-IRS high-resolution spectrum of NGC 2392. The most prominent lines are labeled in the figure.

Fig. 25.— The mid-IR spectrum of a Galactic PN as observed by MIPS on Spitzer. This is Fig. 2 of Pottasch & Bernard-Salas (2008).

Table 5. Electron temperature indicators in NGC 2393.

Ion	Ioniz. Pot.(eV)	Lines Used	Observed Ratio	T_e (K)
[N II]	14.5	5755/6584	0.017	10 000
[S III]	23.3	6312/18.7	0.0.084	12 000
[Ar III]	27.6	7136/21.8	15.8	10 000
[O III]	35.1	4363/5007	0.0165	14 700
[O III]	35.1	1663/5007	0.0496	15 200
[Ne III]	41.0	3869/15.5	1.56	13 500
[O IV]	54.9	1400/25.9	0.44	22 000:
[Ne V]	97.1	3425/24.3	2.2:	25 000

: Indicates uncertain value.
When the wavelength has 4 ciphers it has the units of Angstrom and 3 ciphers is micron.

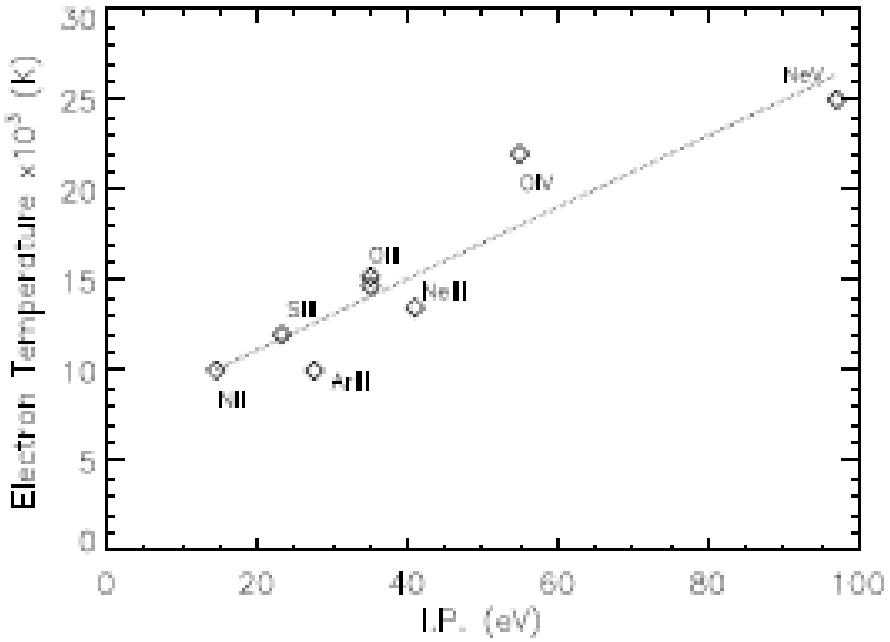

Fig. 3. Electron temperature is plotted as a function of the Ionization Potential.

Fig. 26.— A table of the pairs of lines from a single species in the mid-IR (i.e. in MIPS Spitzer spectra) useful for finding T_e in PN. This is Fig. 3 of Pottasch & Bernard-Salas (2008).

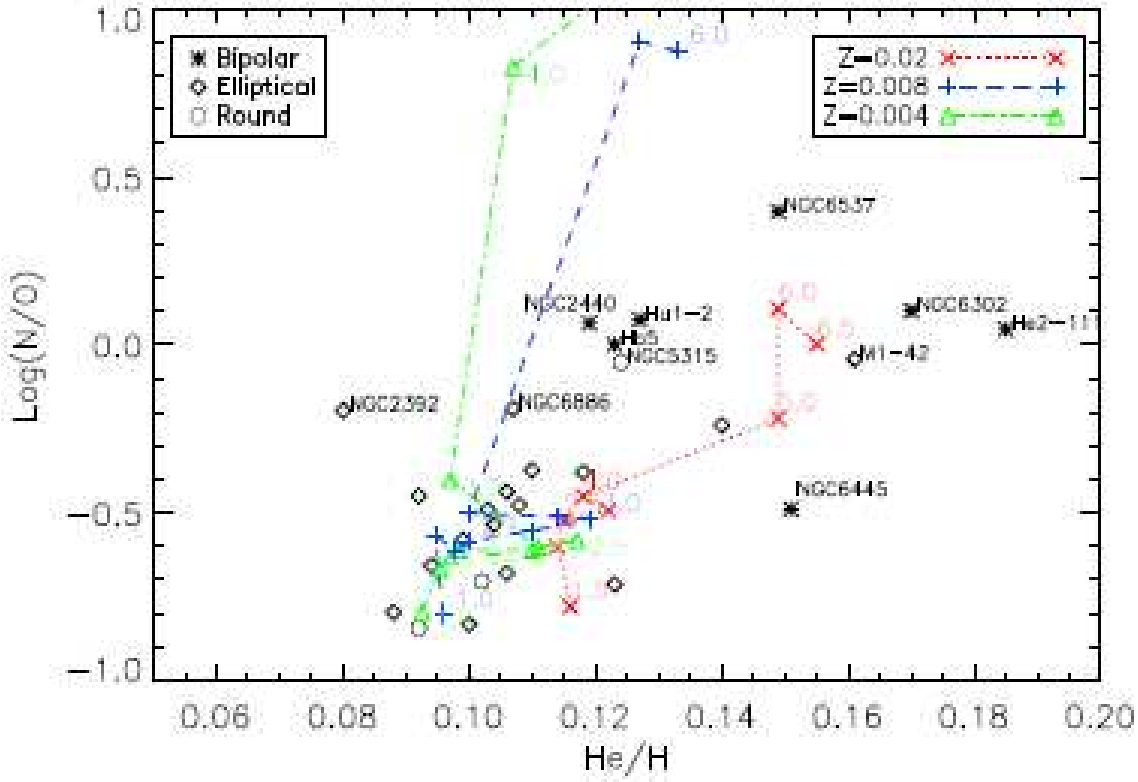

Fig. 2. The N/O abundance ratio is plotted as a function of He/H. The dashed lines connect the results of the models of Karakas for a given value of Z. The ciphers give the initial masses of the individual models. The individual measured PN abundances are from Table 1. Those referred to in the text also have their names given.

Fig. 27.— The ratios N/O vs He/H for a sample of Galactic PN with accurate abundances. The lines are tracks predicted from the AGB models of Karakas. The PN originate mostly from stars of relatively low initial mass for luminous AGB stars, masses near 3 $M_{\odot}$. (Fig. 3 of Pottasch & Bernard-Salas 2010).

2. HII Regions in Local Group Galaxies

Within the Local Group, emission lines from individual HII regions can be detected, and often the ibright ionizing stars (or star clusters) can be resolved by imaging from the ground for the nearer satellites of the Milky Way, or with HST.

Radial metallicity gradients can be measured from planetary nebulae or from HII regions, which indicate the current Z of the ISM. It is difficult to use stellar abundances for this purpose as their spread in metallicity, due to their big spread in age, is too large.

Maciel & Costa (2010, *IAU Symp. 265, Chemical Abundances in the Universe*, see arXiv:0911.3763) review the metallicity gradients in the Milky Way as established by Cepheid variables, HII regions, open clusters, and PN. Average abundance gradients range between -0.03 dex/kpc and -0.10 dex/kpc, with some flattening of the gradients at large galactocentric distances. This, to me at least, suggests that the gradients are better expressed as $dZ/d(logR_{GC})$. The element that can most easily be observed when studying HII regions or PN is oygen. Gradients in the electron temperature inferred from [OIII] lines are also seen. The gradients appear to be slightly steeper for the older objects, implying they flatten somewhat with time.

The LMC and SMC, the two galaxies closest to ours, have a lot of ongoing star formation, and thus have massive clusters with a wide range of ages, some as old as Galactic globular clusters, some much younger. Glatt, Grebel & Koch (2010, see arXiv:1004.1247) give the latest results in an effort dating back more than 40 years to derive the age-metallicity relationship for the LMC and SMC from its clusters. At distances of $\sim$60 kpc, 1/10 that of M31, HST can resolve these clusters, so their ages can be determined from CMDs generated by HST images, while metallicity is from integrated light spectroscopy or photometry. The age distribution of the clusters seems to show a highly variable rate of star formation with time, which may be related to close approaches as these systems orbit the Milky Way.

The most recent attempt to determine the age-metallicity relation for the LMC by Carrera, Gallart, Hardy, Aparicio, & Zinn (2008, AJ, 135, 836) was carried out using an extensive photometric database for field red giants instead of clusters . They found a prompt chemical enrichment, which is predicted by essentially all chemical evolution models for SSP systems, after which the metallicity increased slowly until 3 Gyr ago, when the rate of metal enrichment increased again. The mean metallicity and the MDF are spatially constant until one exceeds a distance more than 6° from the center of the LMC, where the mean Z begins to fall. The star formation rate as a function of time was also studied.

Assuming a solar yield, they can fit the data with a chemical evolution with outflow such that the disk loses the same amount of gas as is ejected by star formation, or by models combining inflow and outflow.

Moving out in distance, there has been a lot of work on M31, especially on its extensive globular cluster system. Merrett, Merrifield, Douglas et al (2006, MNRAS, 369, 120) used a special purpose instrument (the PN Spectrograph) at the William Herschel Telescope in the Canary Islands to detect emission lines from 2165 PN in M31 to study the kinematics of this galaxy. Thousands of star clusters have been cataloged in M31, see Hodge, Krienki, Bianchi, Massey & Olsen (2010, arXiv:1005.2198) for the latest additions, but at the distance of M31 it is much harder to carry out the beautiful CMD studies that one can do for the LMC and the SMC. HST's collecting area is small, and the crowding is fierce even with HST's good spatial resolution. Individual CMDs for M31 clusters, especially for the older ones, require long integrations (many orbits with HST) mto obtain (see Rich, Corsi, Cacciari et al, 2005, AJ, 129, 2670). There are extensive ground based imaging and spectroscopic programs underway to study the halo of M31, with emphasis on the detection of stellar streams.

M31 is a massive galaxy which is highly inclined, so it is not easy to study its HII regions. Instead we move to M33, a nearby fact on galaxy. Rosolowsky & Simon studied

the HII regions there with Deimos/Keck. The metallicity gradient they derive is shown in the appended figure. Bresolin, Stasinsky, Vilchez, Simon & Rosolowsky (2010, see arXiv:1001.4068) extend this work to a smaller sample of 16 PN in M33. The two samples combined give radial gradients of -0.025 ± 0.006 dex/kpc for this galaxy. Bresolin et al (2010) use the PN spectra to establish the production of various elements in AGB stars in M33 as inferred from their descendents, the PN, is similar to that seen in the Milky Way. The figures illustrate how hard this is to carry out; the large scatter seen in these figures is probably largely from observational uncertainties. Magrini, Stanghellini, Corbelli, Galli & Villaver (2010) use all this data plus their own for M33 to try to determine the age-metallicity relation for M33. They point out the in the central region of M33 Z is apparently lower than just outside it, a problem which they ascribe to observational sample bias.

One sees from this summary that the regime over which such studies can be pursued, even in this age of 10-m telescopes, is restricted to the Local Group. More distant galaxies means larger observational uncertainties, lousy S/N spectra, and an inability to constrain models of chemical evolution very much.

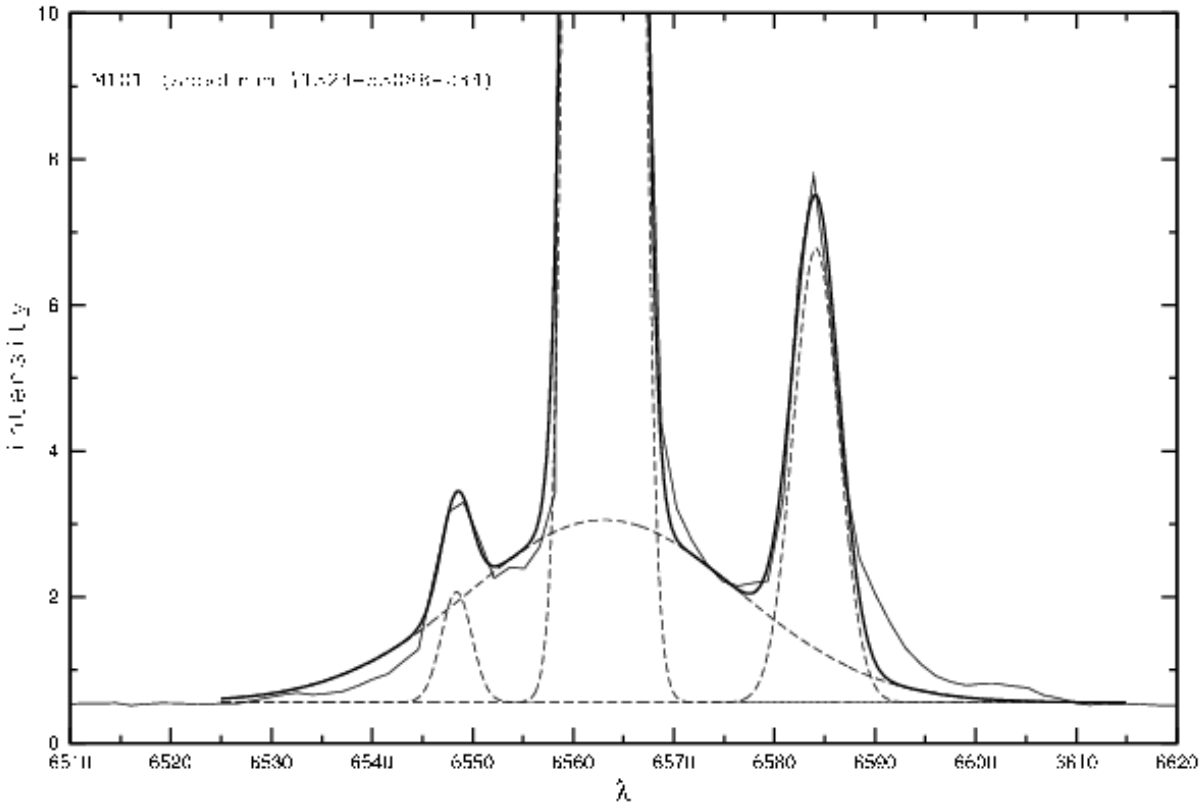

Fig. 1.— Example of a fit to the [NII]λ6548, Hα (both narrow and broad components) and [NII]λ6584 line profiles. We show here the spectrum # 1324-53088-234 of an H II region in the disk of the spiral galaxy M101. The thin solid line is the observed spectrum, the thick solid line is the fit to it, and the dashed lines are fits to individual lines.

Fig. 28.— Fig. 1 of Pilyugin & Thuan (2007, ApJ, 669, 299).

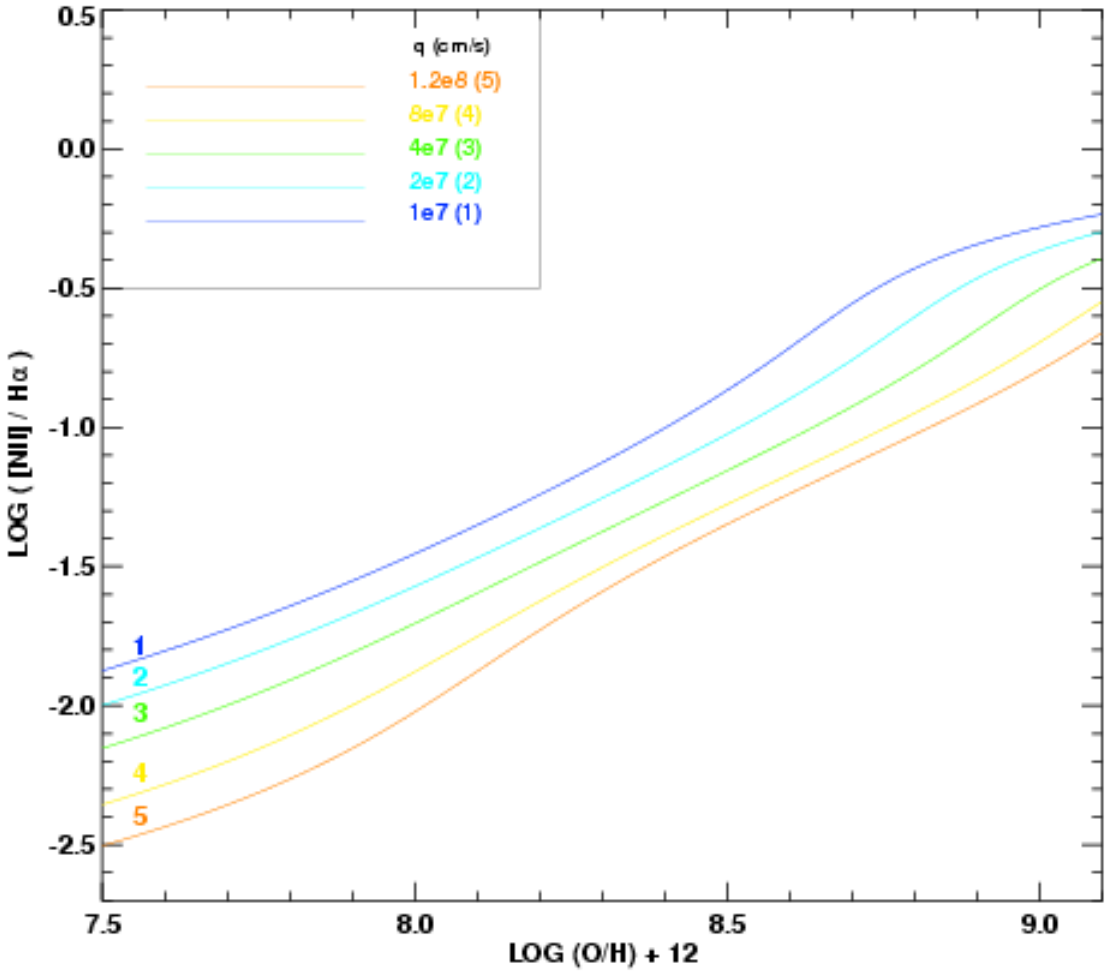

Fig. 4.— The metallicity-sensitive line ratio [N II]/Hα versus the metallicity $12 + \log(O/H)$. The colored curves show our new parameterization (equation 12) to the theoretical photoionization models of Kewley & Dopita (2003) for various values of ionization parameter, q, in cm s^{-1} shown in the legend. Note that the [N II]/Hα ratio is very sensitive to ionization parameter and is a not a robust indicator of metallicity. The metallicity corresponding to any particular value of [N II]/Hα spans 0.4—0.6 dex in O/H, depending on ionization parameter.

Fig. 29.— Fig. 4 of Kobulnicky & Kewley (2004, ApJ, 617, 240).

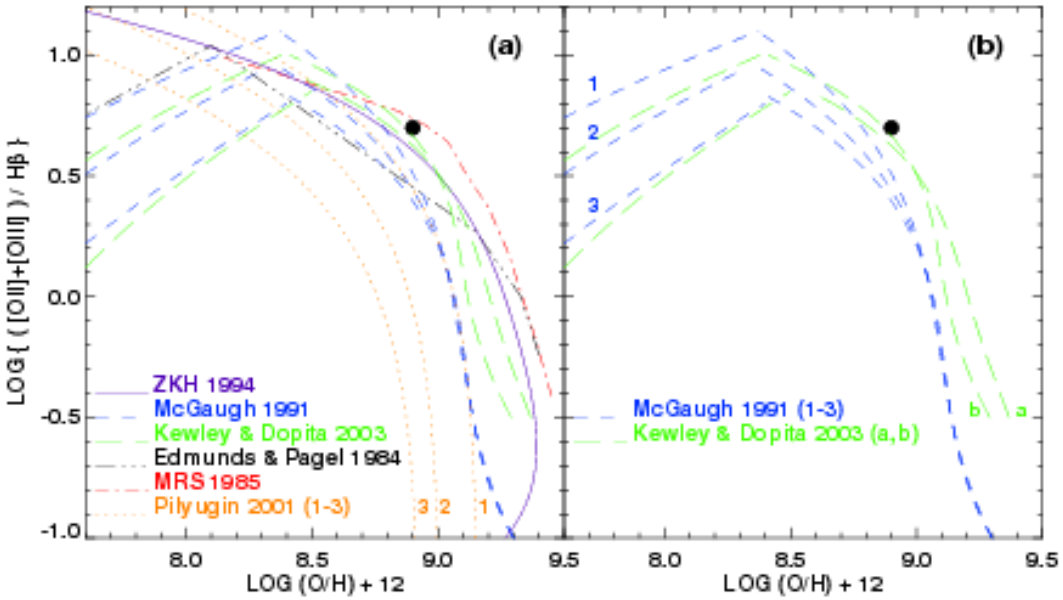

Fig. 6.— Metallicity calibration between strong line ratio R_{23} and oxygen abundance, $12+\log(O/H)$ from several different authors as indicated in the legend. A solid circle marks the Orion Nebula value (based on data of Walter, Dufour, & Hester 1992). For reference, the currently accepted value of solar abundance is $12+\log(O/H)_{\odot} = 8.7$ (Allende Prieto, Lambert, & Asplund 2001). Panel (a) shows the variation in R_{23} calibrations from the literature, while panel (b) shows the M91 and KD03 calibrations. The three curves labeled 1,2,3 denote the Pilyugin 2001 and M91 models corresponding to $\log(O_{32}) = 1, 0, -1$ respectively. Two curves labeled a,b denote the Kewley & Dopita (2003) models corresponding to ionization parameters of $q = 1 \times 10^7$ and $q = 1.5 \times 10^8$ cm/s respectively.

Fig. 30.— Fig. 6 of Kobulnicky & Kewley (2004, ApJ, 617, 240).

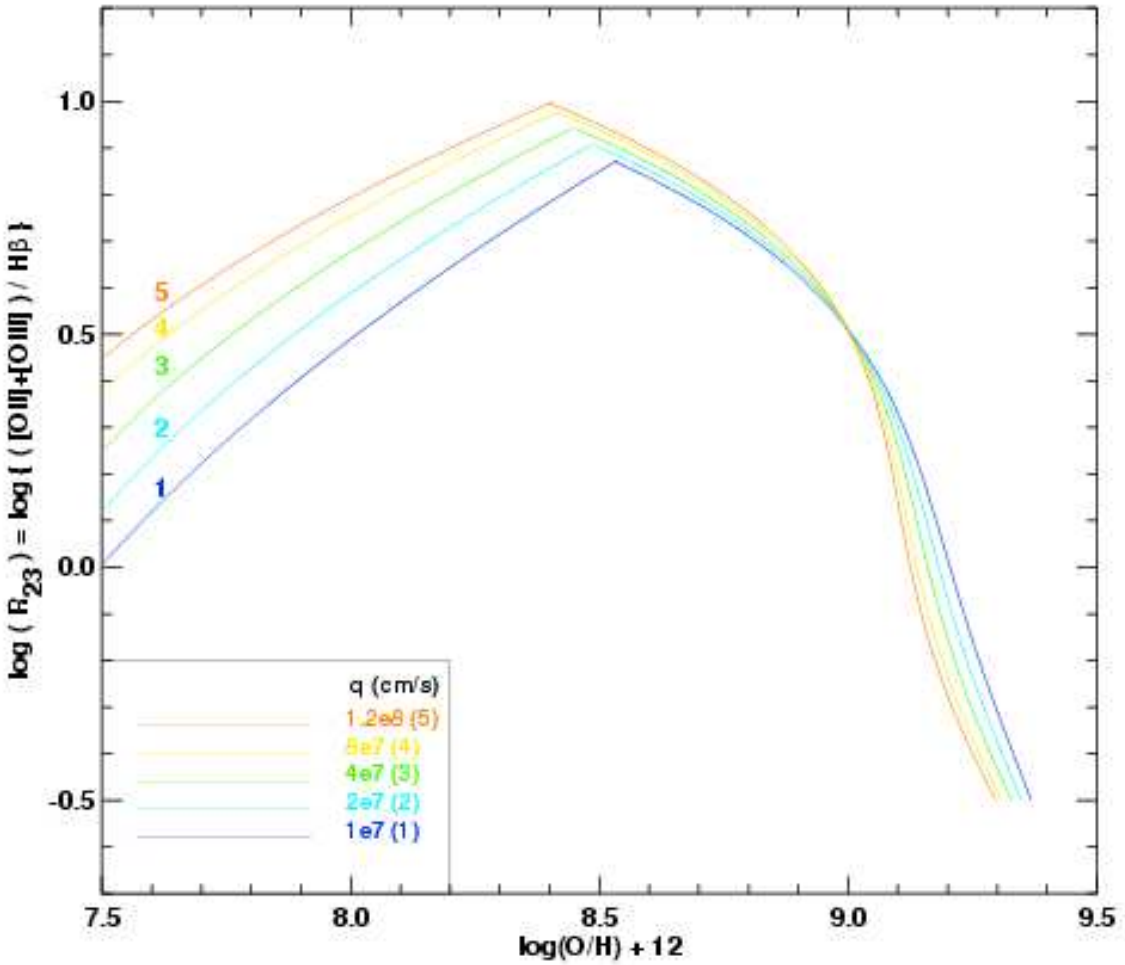

Fig. 7.— The metallicity-sensitive line ratio R_{23} versus the metallicity $12 + \log(O/H)$. The colored curves show our new parameterization (equation 17) to the theoretical photoionization models of Kewley & Dopita (2003) for various values of ionization parameter, q, in cm s^{-1} shown in the legend.

Fig. 31.— Fig. 7 of Kobulnicky & Kewley (2004, ApJ, 617, 240).

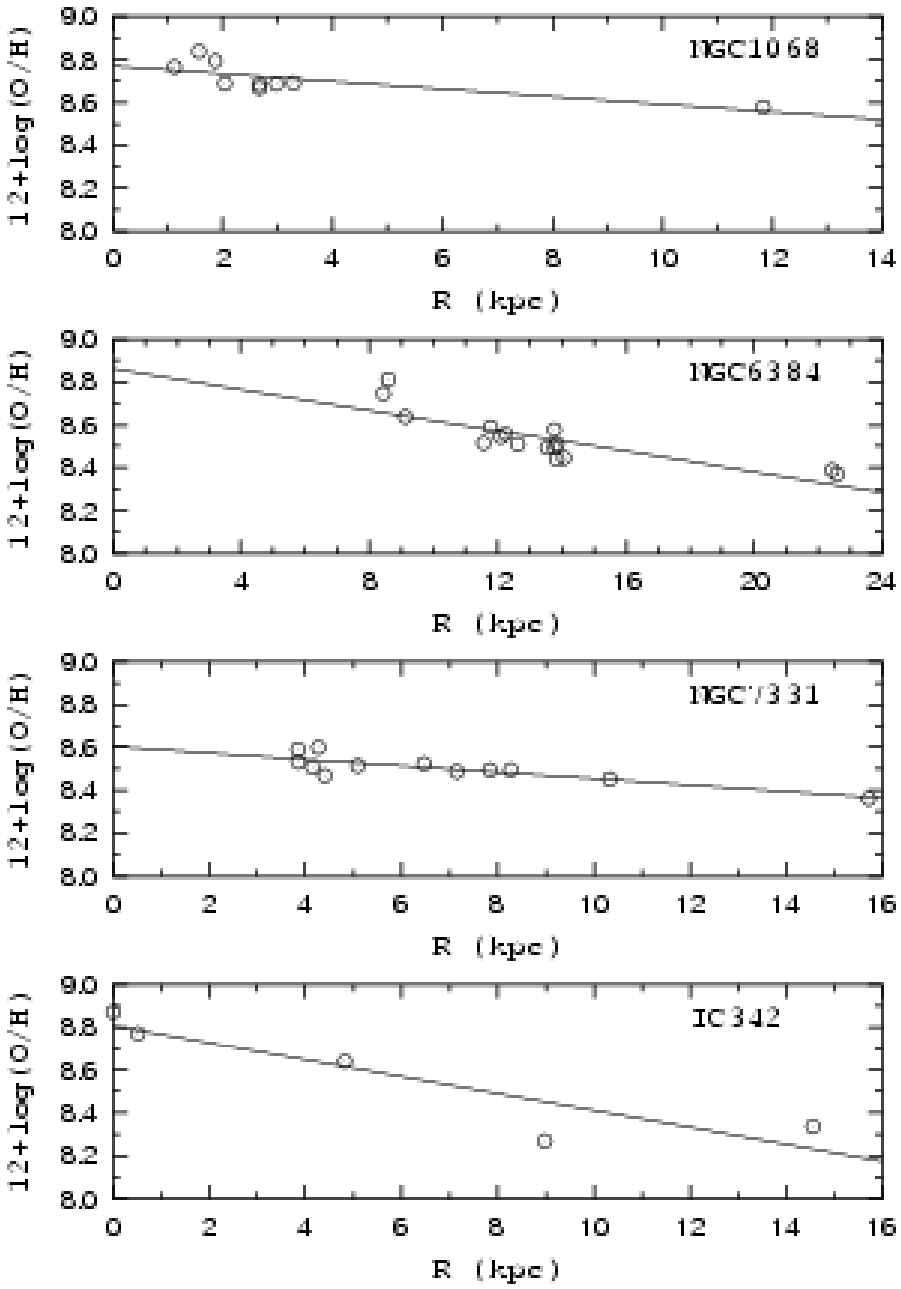

Figure 1. The oxygen abundance as a function of galactocentric distance in the disks of the four most luminous spiral galaxies in our sample: NGC 1068, NGC 6384, NGC 7331 and IC 342. The circles are $(O/H)_{ff}$ abundances in individual H II regions. The lines are linear least-square best fits to those data points.

Fig. 32.— Fig. 1 of Pilyugin, Thuan & Vilchez, (2007, MNRAS, 376, 353). Radial metallicity gradients inside local late-type galaxies.

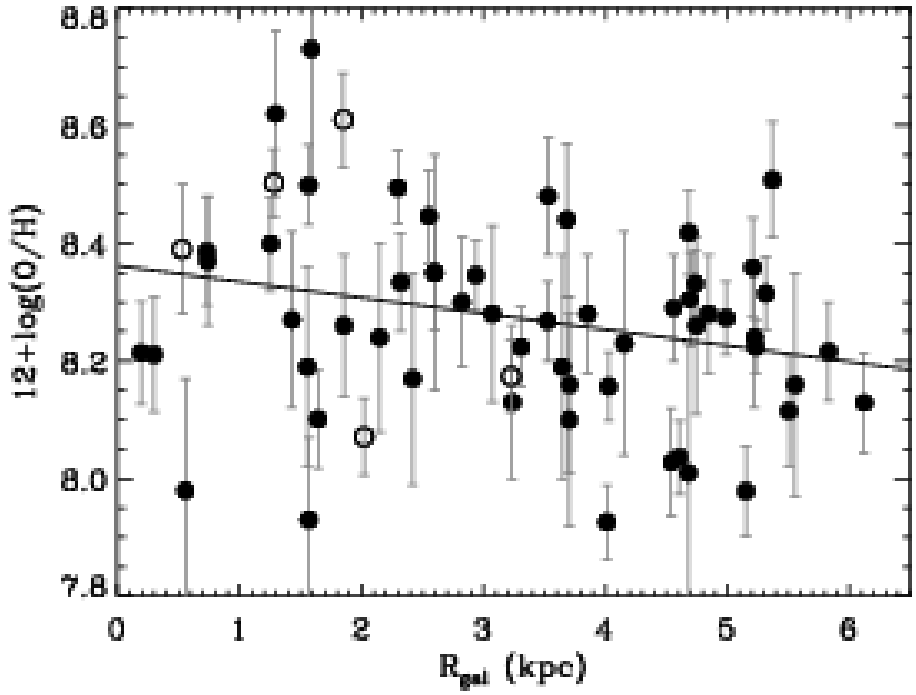

FIG. 2.— Abundances of 61 H II regions in M33 as a function of galactocentric radius. A linear gradient with a slope of −0.027 dex kpc^{-1} is fit to he data (solid line). Regions with significant He II λ4686Å emission are ndicated with open symbols.

Fig. 33.— Fig. 1 of Rosolowsky & Simon, (2008, ApJ, 675, 1213), who studied the emission line spectra of 61 HII regions in M33 to derive O abundances.

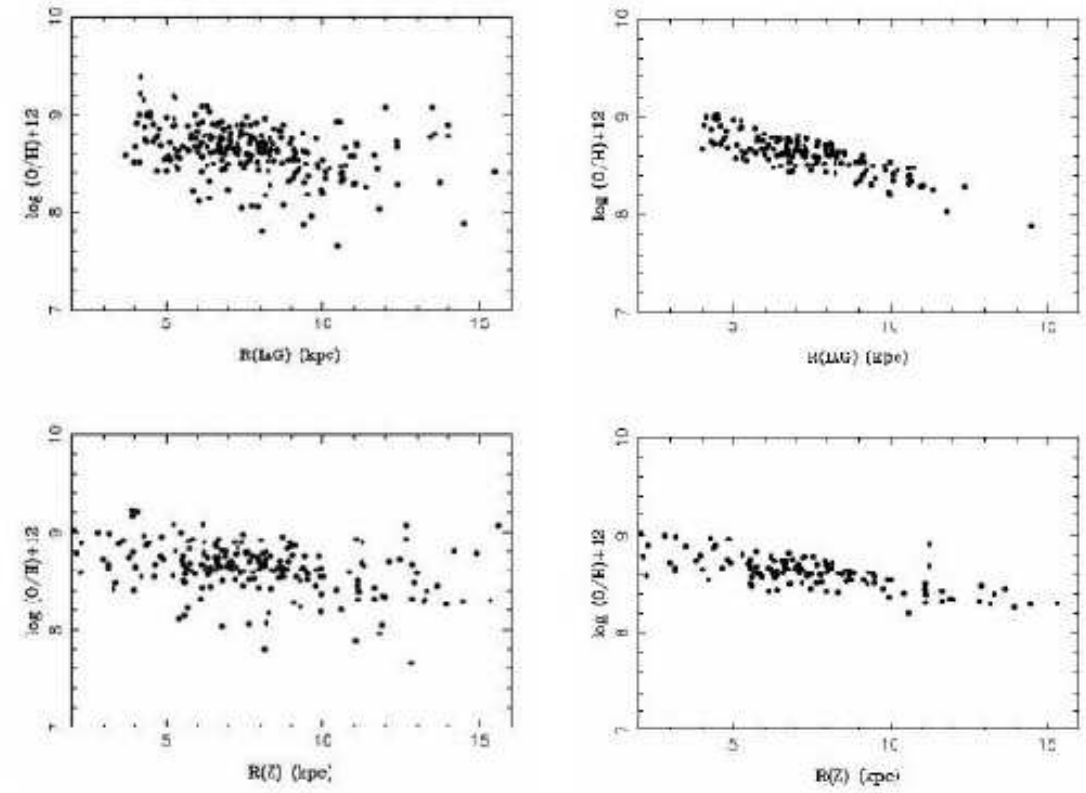

Figure 1. The O/H radial gradient from PN. Top: Distances from the IAG/USP group, Bottom: Distances from Stanghellini et al. (2008). Left: CSPN with ages in the range 2–10 Gyr; Right: CSPN with ages in the range 4–6 Gyr.

Fig. 34.— Radial gradients in the disk of the Milky Way determined from planetary nebulae, as reviewed by Maciel & Costa (2010, *IAU Symp. 265, Chemical Abundances in the Universe*, their Fig. 1).

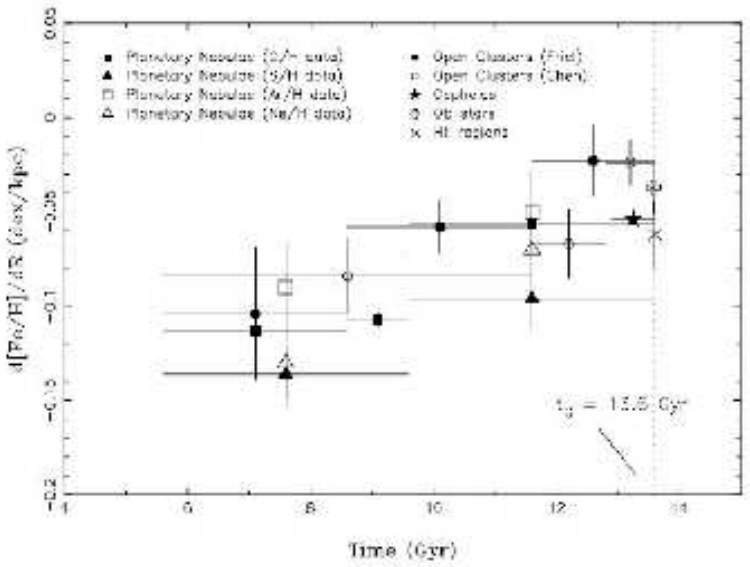

Figure 2. Time variation of the radial abundance gradient (Maciel & Costa 2009).

Fig. 35.— The variation with time of the slope of the radial gradient in the disk of the Milky Way can be roughly determined using age estimates for various open clusters. Fig. 2 of Maciel & Costa (2010).

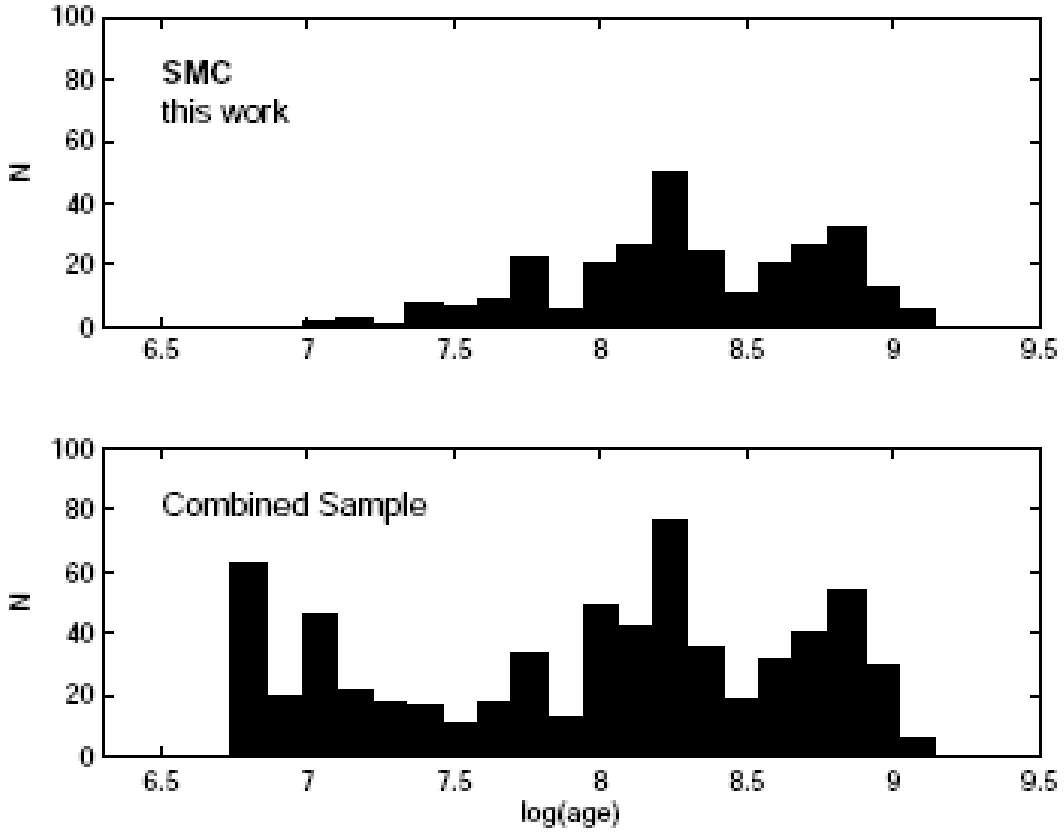

FIG. 5.— Cluster age distribution of the SMC. The age distribution derived in this study (upper panel) and the combined samples (lower panel) of this study and C06 are shown (in total 821 clusters). Only the most reliable ages were considered for this plot (classes 1 and 2 in Table 1).

Fig. 36.— The cluster age distribution for the LMC and SMC, with a total of 821 clusters included. Fig. 5 of Glatt, Grebel & Koch (2010).

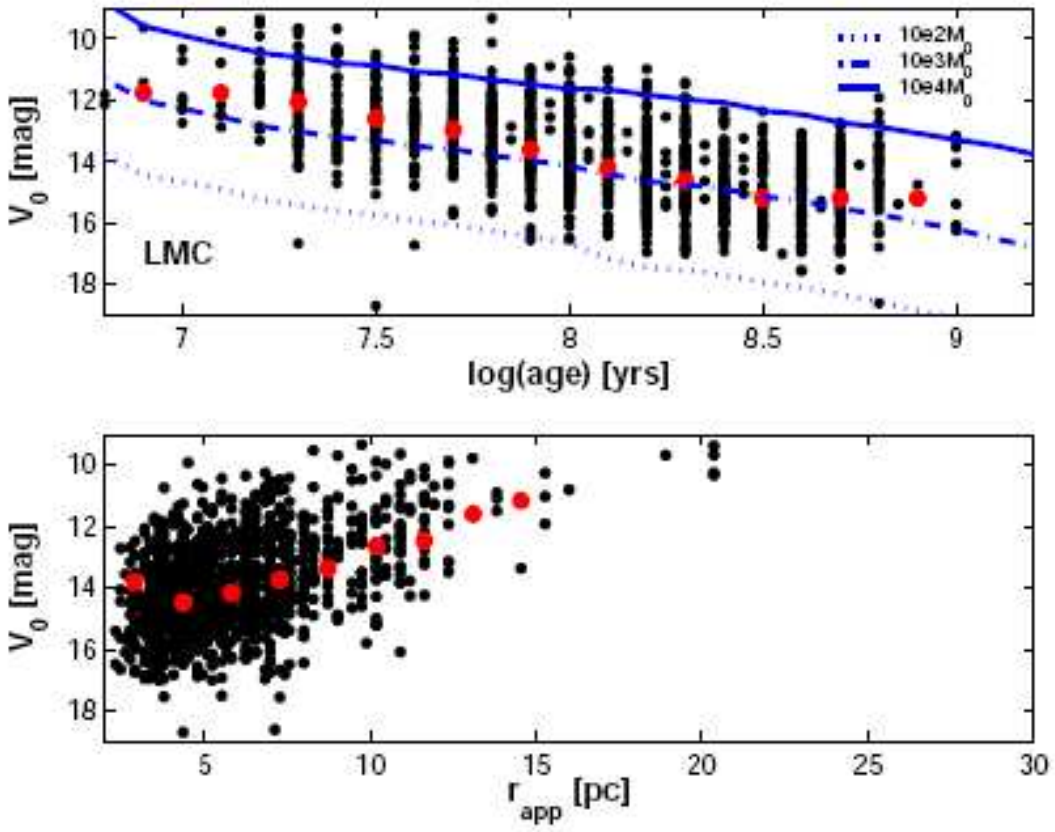

FIG. 14.— V_0 vs log(age) and V_0 vs apparent overall radius relations for our LMC clusters. The luminosities were derived in this study. The red dots represent the mean of the age distribution in magnitude bins of 0.3 mag. The trend for fainter magnitudes with increasing age is also obvious in this plot. The blue lines represent three GALEV models (Kotulla et al. 2009) of different total mass: $10^4 M_\odot$ (solid), $10^3 M_\odot$ (dash-dotted), and $10^2 M_\odot$ (dotted).

Fig. 37.— The cluster age vs V_0 (V corrected for reddening) distribution for the sample in the LMC, which is Fig. 14 of Glatt, Grebel & Koch (2010). The blue lines in the upper panel represent SSP predictions for a fixed mass of 10^4, 10^3 and $10^2 M_\odot$ yr, fading with time as the stellar population ages. Such models are a good fit to the mean of the observations.

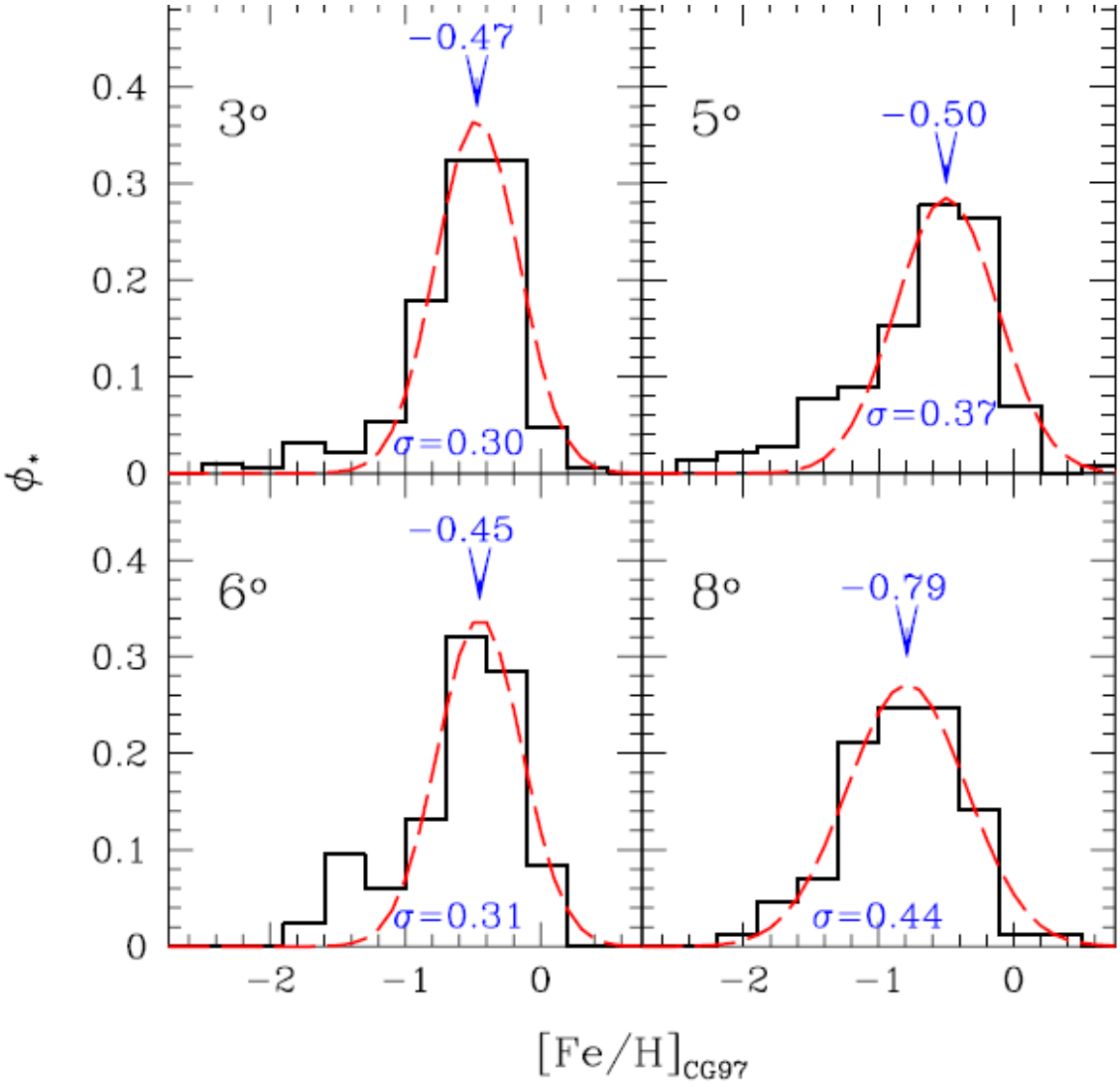

Fig. 5.— Metallicity distributions for the four fields in our sample. A Gaussian has been fitted to each distribution in order to obtain its mean and dispersion. The values obtained are shown in each panel.

Fig. 38.— The metallicity distribution for four fields in the LMC. Only for the outermost field does $< [Fe/H] >$ drop somewhat. This is Fig. 5 of Carrera et al (2008).

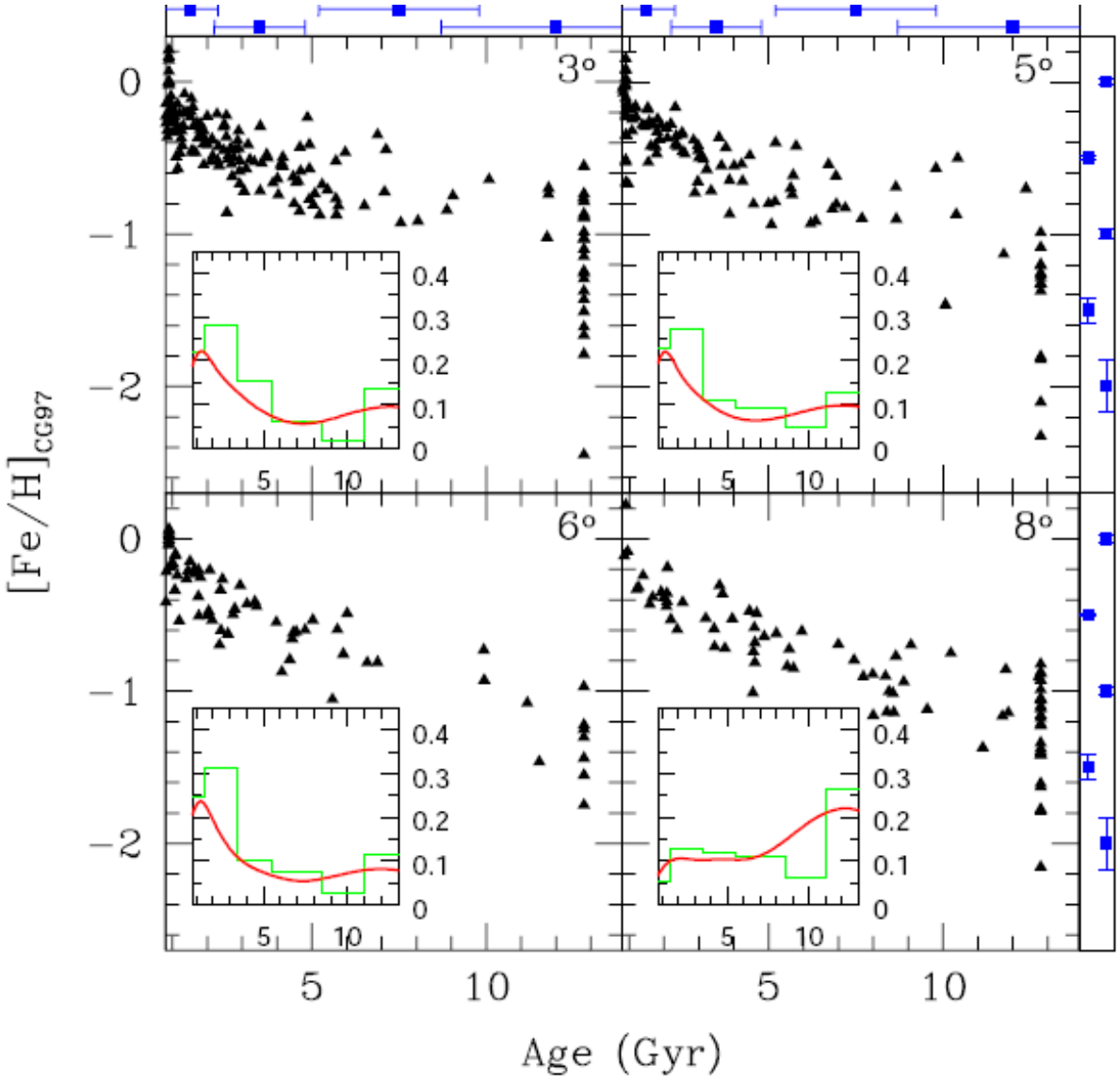

Fig. 11.— Age–metallicity relationships for the four LMC fields in our sample. Inset panels show the age distribution computed taking into account (*solid line*) and not (*histogram*) the age determination uncertainties. The top panel show the age error in each interval. The left panels show the metallicity error.

Fig. 39.— The metallicity distribution for four fields in the disk of the LMC. This is Fig. 11 of Carrera et al (2008). Note the large prompt enrichment among the oldest objects.

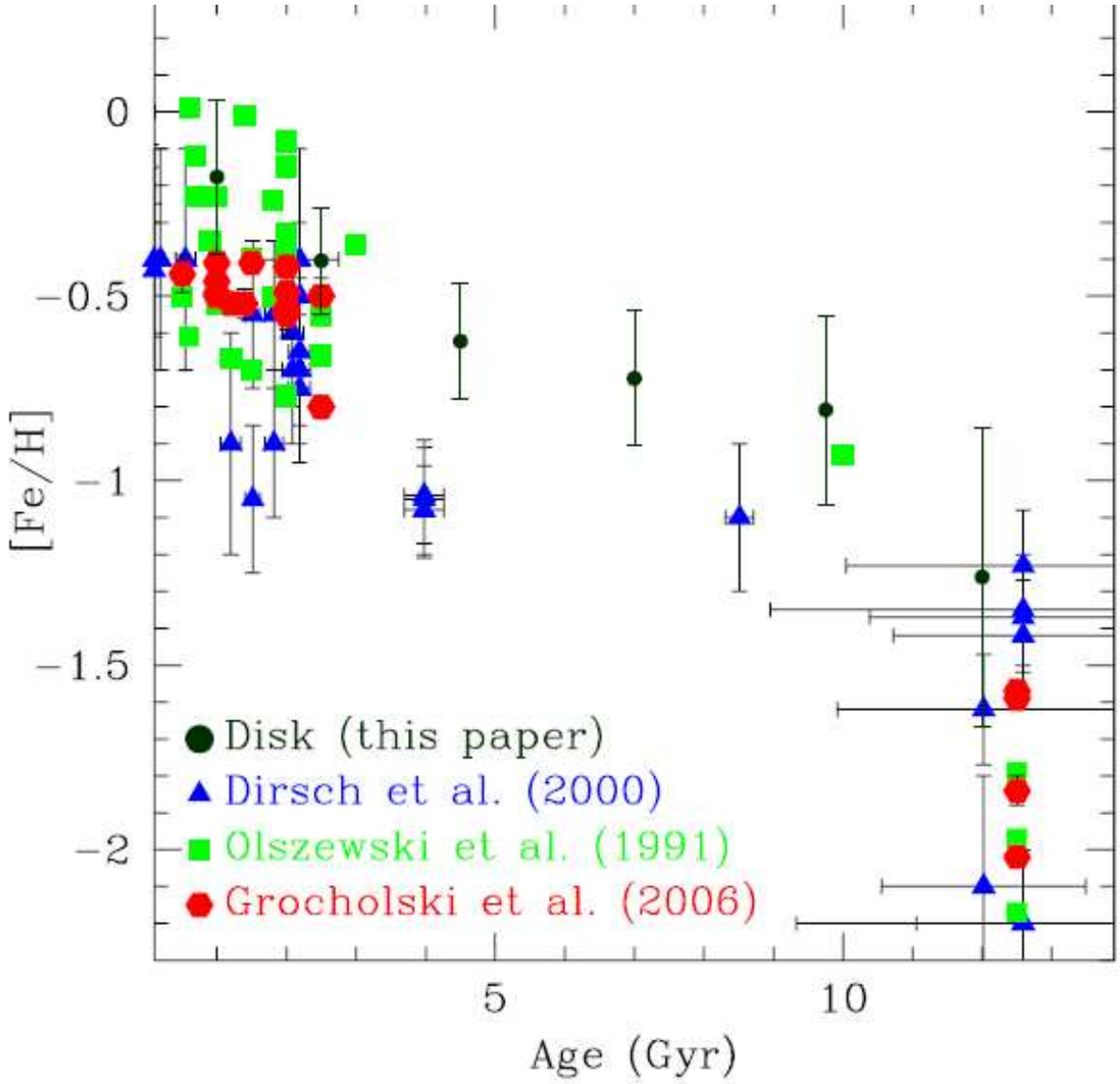

Fig. 14.— LMC clusters AMR by Olszewski et al. (1991, *squares*); Dirsch et al. (2000, *triangles*) and Grocholski et al. (2006, *hexagons*). The mean metallicity in six age bins of our global disk has been plotted (*filled points*). Note that the metallicity scales of each work may not be exactly the same.

Fig. 40.— The metallicity distribution for four fields in the disk of the LMC compared to those derived from several studies of LMC clusters. This is Fig. 14 of Carrera et al (2008). Note the large prompt enrichment among the oldest objects.

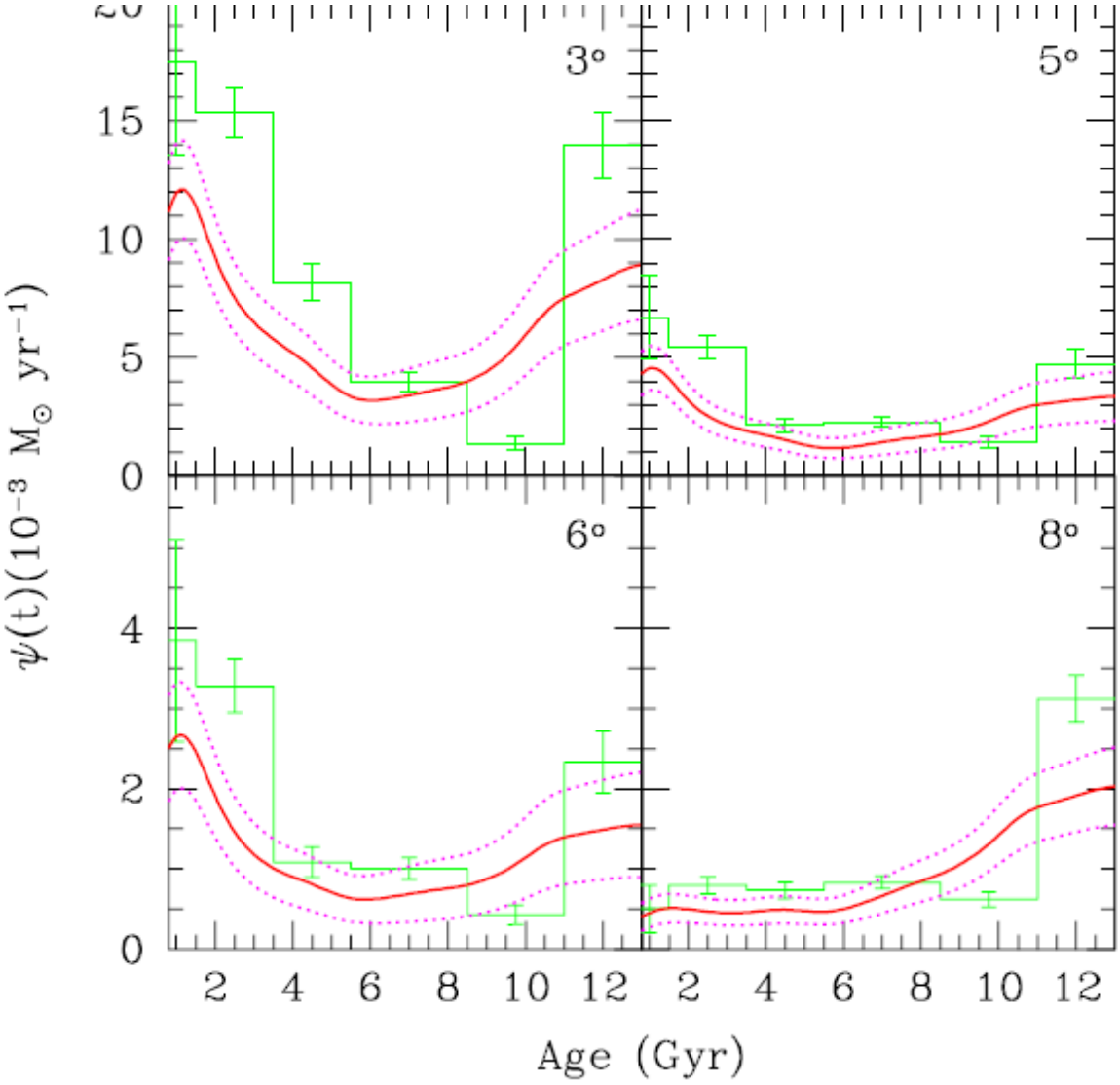

Fig. 16.— SFR, as a function of time, for our four fields. Note that the y-axis scale is different in the top and bottom panels. Histogram is the $\psi(t)$ computed from the age distribution without taking into account the age uncertainty. Solid line is the same but computed by taken into account the age error, while dotted lines are its uncertainty.

Fig. 41.— The star formation rate as a function of time in the LMC field. This is Fig. 16 of Carrera et al (2008).

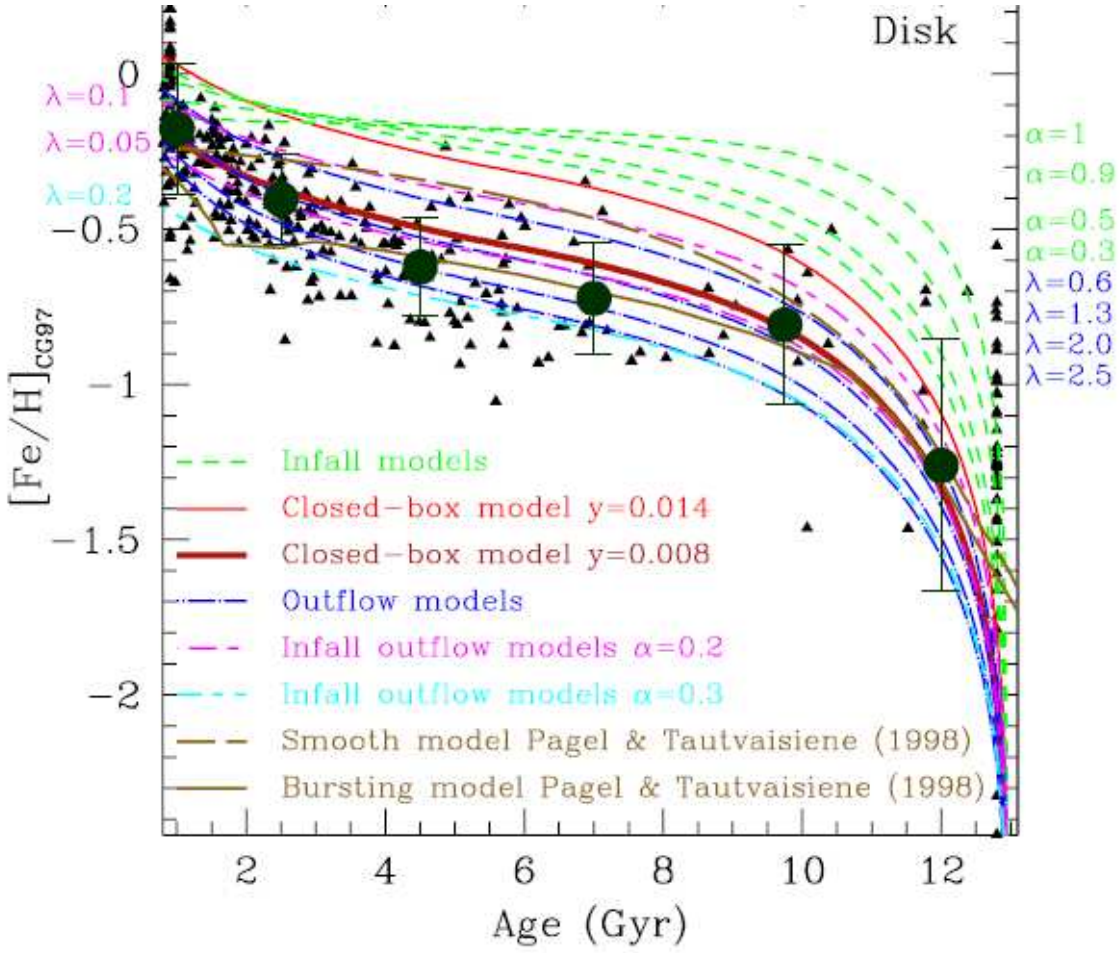

Fig. 18.— Chemical evolution models overplotted on the AMR for the disk. Red solid lines are the closed-box models with $y = 0.008$, (*thick line*) and $y = 0.014$ (*thin line*), respectively. Blue dot-dashed lines are outflow models for $\lambda = 0.6$, 1.3, 2.0 and 2.5. Green dashed lines are infall models with $\alpha = 1$, 0.9, 0.5 and 0.3. Pink long–short dashed lines are models with infall and outflow for $\alpha = 0.2$, and $\lambda = 0.1$ (*upper*) and 0.05 (*lower*). Finally, cyan short-long dashed line is a model with inflow and outflow for $\alpha = 0.3$ and $\lambda = 0.2$. All infall and outflow models assume $y = 0.014$. The brown solid and dashed lines represent the bursting and smooth models computed by Pagel & Tautvaisiene (1998).

Fig. 42.— The age-metallicity relation for the LMC compared to various models of chemical evolution including a closed box, outflow models, infall + ouflow, and possible bursting star formation. Note the difficulty of distinguishing between the various models given the size of the error bars on each of the 6 age bins. This is Fig. 18 of Carrera et al (2008).

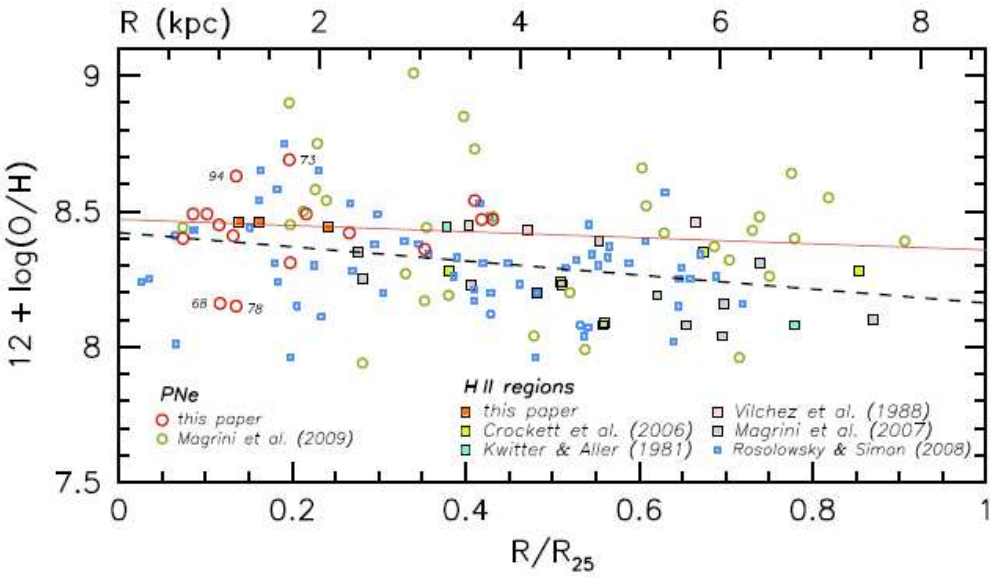

Figure 15. O/H radial gradient for PNe and H II regions. Radial distances are given both in terms of the isophotal radius R_{25} (bottom axis) and in kpc (top axis). The different symbols used are summarized in the legend. Linear regressions are shown by the red continuous line (PNe) and the dashed black line (H II regions). The four planetaries that deviate the most from the PNe regression, PN 68, 73, 78 and 94, are labeled.

Fig. 43.— The radial gradient in oxygen found from PN and HII regions in M33. This is Fig. 15 of Bresolin et al (2010).

3. Galaxy Luminosity and Central Metallicity

A common theme in galaxy studies is the correlation between galaxy total luminosity and central metallicity. Luminosity can be taken as a crude proxy for total mass, particularly if one avoids the bluer regions of the spectrum, where small age and metallicity differences can influence the emitted integrated flux. This correlation presumably arises from one of several causes – first, a more massive galaxy has a higher binding energy, and can more easily retain ejecta from SN. In low mass galaxies, freshly enhanced metal rich gas may more readily be lost through galacitic winds. The second cause may be related to the role of central AGNs, whose mass is also strongly correlated with the mass of the bulge component of the galaxy. These issues will be discussed in more detail in the section on absorption lines in galaxies.

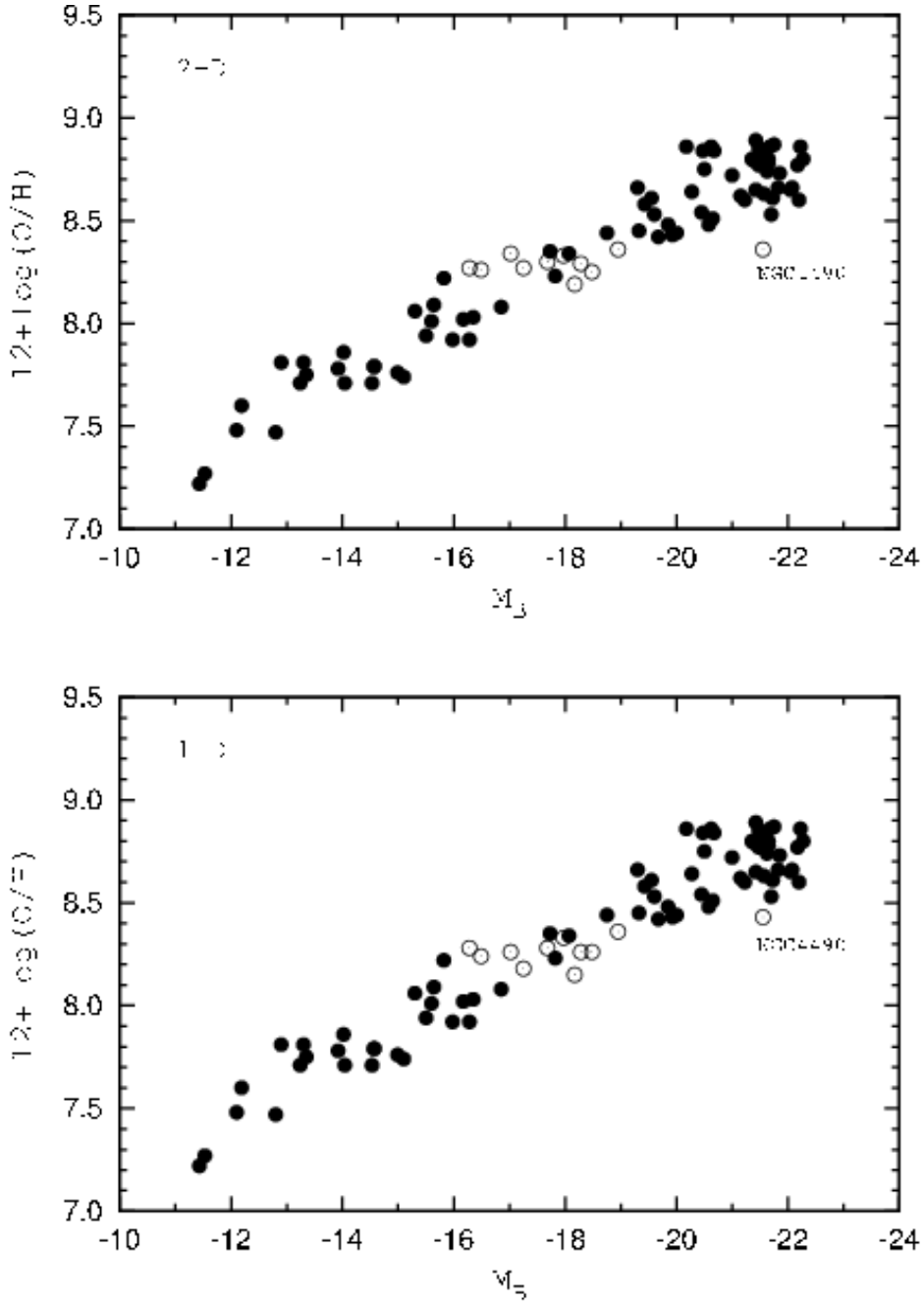

Fig. 44.— Fig. 10 of Pilyugin & Thuan (2007, ApJ, 669, 299). Luminosity - central metallicity diagram for nearby galaxies with spectra of at least one HII region in the SDSS database and with a detected 4363 Å [OIII] line using two different procedures to overcome the problem that the wavelength range of the SDSS does not include the 3727 Å line of [OII].

Suggested Reading:

Kewley & Ellison, 2008, ApJ, 681, 1183 Metallicity Calibrations and the Mass-Metallicity Relation for Star-Forming Galaxies (calibration of Mass-metallicity relation and application to star-forming galaxies $z < 0.1$ in SDSS.

Kewley, Groves, Kauffman, Heckman, 2006, MNRAS, 372, 961 The Host Galaxies and Classification of AGN

Pilyugin & Thuan, 2007, ApJ, 669, 299 O Abundance of Nearby Galaxies from SDSS spectra

Pilyugin, Thuan & Vilchez, 2007, MNRAS, 376, 353 Maximum value of cosmic O abund and O yield

C. Leitherer - Spectral Evolution Models for the Next Decade, 2010, in *Stellar Populations – Planning for the Next Decade*, arXiv:0910.1327

D. Osterbrock, classic book, *Astrophysics of Gaseous Nebulae and Active Galactic Nuclei*